NTNU – Trondheim
Norwegian University of
Science and Technology

Developing Methods and Tools for Three-Dimensional Computational Reconstructions in X-ray and Visible Light Microscopy

Torbjørn Kringeland

MSc in Physics
Submission date: May 2015
Supervisor: Dag Werner Breiby, IFY

Norwegian University of Science and Technology
Department of Physics

Abstract

In this thesis possibilities for further developments in microscopy have been explored. This was done through two sub-projects: The first project was on small-angle X-ray (SAXS) tomography, and the second revolved around optical microscopy combined with computations. Both projects make use of numerical methods to computationally reconstruct sample properties in three dimensions. Even though the projects are concerned with different ranges of the electromagnetic spectrum, they both have relevance for X-ray microscopy.

In the project on SAXS tomography it was investigated if the orientation distribution of talc particles in a sample of injection molded isotactic polypropylene could be retrieved by using the scattering patterns from tomography experiments. In traditional computational tomography (CT) attenuation contrast can be used to reconstruct the attenuation properties of a sample. New synchrotron and detector technologies have made it possible to observe scattering contrast from sub-micron scale objects. Currently no method exists to retrieve the spatially varying three-dimensional orientation distribution of these objects if the scattering contrast depend on their orientation, without physically cutting the sample. To retrieve the orientation distribution of the talc particles the numerical method of simulated annealing was used. By utilising prior knowledge of the sample and the scattering patterns, various alterations of the energy function have been investigated as possibilities to improve the results. The main features of the orientation distribution were obtained, with some of the finer details that have previously been observed in experiments on a physically cut sample. This shows great promise for further studies on SAXS tomography, and the results achieved in this thesis will be published [1].

In the other sub-project, dealing with light microscopy, a varied-illumination microscope to be used as a research and educational tool, was constructed. Developments of new advanced techniques in microscopy often make demands of increasingly complex and expensive high-quality equipment. In

X-ray microscopy this often means the experiments have to be carried out at large synchrotrons, where higher brilliance and coherence can be achieved. Recent developments in visible light microscopy have shown that it is possible to create a small microscope with a wide range of imaging capabilities, by replacing the conventional back light illumination scheme with a programmable LED array, combined with computer based image processing, post exposure. Of particular interest is its ability of Fourier Ptychography, which is an adaptation of Ptychography which is increasingly used with X-ray microscopes. Our microscope is demonstrated to be able to form bright and dark field images, by post processing on the same data set. By utilising the variable-illumination features of the microscope, images deliberately taken out of focus have successfully been digitally refocused by computational reconstructions. The microscope offers highly versatile hardware and software, with already planned future projects on Fourier Ptychography and three-dimensional surface reconstruction of polymer micro-beads during mechanical compression in mind.

Sammendrag

I denne avhandlingen har muligheter for videreutvikling innen mikroskopi blitt undersøkt. Dette ble gjort i form av to delprosjekter: Det første prosjektet var om småvinkelrøntgenspredningtomografi (SAXS tomografi), og det andre tok for seg optisk mikroskopi med beregninger. Begge prosjektene tar i bruk numeriske metoder for å rekonstruere prøver i tre dimensjoner. Selv om prosjektene tar for seg forskjellige deler av det elektromagnetiske spekteret, så har begge relevans for røntgenmikroskopi.

I SAXS tomografi prosjektet ble det undersøkt om orienteringsfordelingen av talkpartikler i en prøve av sprøytestøpt isotaktisk polypropylen kunne finnes ut fra spredningsdata fra tomografieksperimenter. I tradisjonell beregningstomografi (Computed Tomography) kan absorbsjonskontrast brukes for for å rekonstruere absorbsjonskoeffisienten inni prøven. Ny synkrotron og detektor teknologi har gjort det mulig å observere spredningskontrast fra submikrometer store objekter. Per i dag finnes det ingen måte å finne den romlig varierende orienteringsfordelingen av disse objektene dersom spredningskontrasten varierer med orienteringen, uten å fysisk kutte prøven. For å finne orienteringsfordelingen til talkpartiklene ble den numeriske metoden *simulert nedkjølning* (Simulated Annealing) brukt. Ved å utnytte tidligere kunnskap om prøven og spredningsmønstrene, har forskjellige endringer av energifunksjonen blitt undersøkt som muligheter for å forbedre resultatene. Hovedtrekkene av orienteringsfordelingen kan observeres, sammen med noen av de finere detaljene som har blitt observert i tidligere eksperimenter på fysisk kuttede prøver. Dette viser at det er gode muligheter for videre studier på SAXS tomografi, de oppnådde resultatene i denne avhandlingen vil bli publisert [1].

I det andre delprosjektet, som tok for seg lysmikroskopi, ble det bygget et variert-belysning mikroskop som skal brukes som et vektøy innen forskning og utdanning. Nye utiklinger innen mikroskopi krever stadig mer komplekse og dyrere høykvalitetutstyr. Innen røntgenmikroskopi resulterer dette ofte i at eksperimenter må gjøres på synkrotroner, hvor høyere brillians

og koherens kan oppnås. Nylig har det blitt vist at det er mulig å lage et lite mikroskop som har en rekke avbildningsmuligheter, ved å bytte ut den vanlige bakbelysningen med et programmerbart LED brett, kombinert med beregningsbasert bildebehandling etter eksponering. Spesielt interresant er mikroskopets evne til å kunne brukes til Fourier Pthychografi, som er en tilpasning av Ptychografi som stadig brukes mer innen røntgenmikroskopi. Vårt mikroskop har demonstrert evnen til å skape "bright field" og "dark field" avbildning, ved etterprosessering av det samme datasettet. Ved å utnytte den variert-belysning egenskapen til mirkoskopet, har bilder som med overlegg har blitt tatt utav fokus blitt refokusert ved bruk av beregningsbasert digitale rekonstruksjonsmetoder. Mirkoskopet har allsidig maskin og programvare, slik at det kan brukes i allerede planlagte prosjekter på Fourier Ptychografi og tre-dimensjonal overflaterekonstruksjon av mirokompositter under mekanisk komprimering.

Preface

This thesis is the concluding part of a tow years Master of Science degree in Physics at the Norwegian University of Science and Technology (NTNU). The degree was conducted from August 2013 to May 2015. It consist of 120 credits where 60 of these are from this thesis. This thesis consist of two smaller projects that were both done as part of the X-ray group at the Department of Physics at NTNU. The first project was on small-angle X-ray (SAXS) tomography, and the second to build a varied-illumination microscope (VIM). Both projects are related to ongoing research in the field of condensed materials.

I would like to thank my supervisor Professor Dag Werner Breiby for his guidance and invaluable insight.

The experimental data used in the SAXS tomography project was measured at the Swiss Light Source (SLS) in 2012 by Dr. Håvard Granlund, Dr. Kristin Høydalsvik and Professor Dag Werner Breiby with assistance from the staff at the SLS. I would like to thank anyone involved in the experiments. In addition a special thanks to Eirik Torbjørn Bakken Skjønsfjell for giving access to his previous work on SAXS tomography in addition offering to his time and continuous assistance on both projects.

The VIM project was built in the in-house lab of the X-ray group at NTNU. An additional thanks should be handed out to Ole Tore Buset, engineer at the Department of Physics for his assistance in building the microscope and ability to come up with constructions from handwaving explanations. The copper grids used for refocusing were provided by the TEM group at the Department of Physics at NTNU, and I would like to thank them for their donation. The microscope gave me the opportunity of investigating the technical details behind the electronics and tailor my own specialized software on top of performing my own experiments and analysis. It was built as both a research and educational tool. I hope future users find great use of it.

Finally I would like to thank my family. Even if they do not understand a thing of what I say, they still pretend to be interested in what I do.

Table of Contents

List of Figures

Chapter 1

Introduction

1.1 Light based Microscopy

The refraction of light by matter has been known for millennia, however the first light microscope was first developed 400 years ago, and it is intriguing how little is has developed in design since then. This might partially be due to the equation stated by Ernst Abbe in 1873 which says that the highest resolution that can be achieved by light is about a half of its wavelength. Since the limits were put on the hardware a lot of research has been done to improve the components of the microscope to reduce aberrations in order to let the limiting factor be Abbe's formula. Wilhelm Röntgen took the famous first X-ray image in 1895. However the X-rays ability to non-destructively penetrate matter set the stage for a whole new field of research at the interior of samples. A wide range of X-ray diffraction and imaging methods have been developed, and the use of X-rays in both medical and material sciences is well established.

1.2 SAXS Tomography

One of the widely used methods developed for X-rays was Computational Tomography(CT) by Allan Cormack and Godfrey Hounsfield, which allows for three-dimensional nondestructive imaging of material interiors. They developed the first prototype CT machines and were awarded with the Nobel prize in medicine in 1979 for their work. CT uses linescans at

various angles of the sample to digitally reconstruct a cross section of the sample. Most people are familiar with CT from its use in hospitals. The *attenuation* of X-rays is different in various organs which makes it possible to detect organ defects and tumours, and this method of three dimensional reconstructions is well explored. Only in recent years has it been made possible to reconstruct features of the sample using the *scattered* X-ray signal and not only the attenuation of the direct beam. This is due to the development of better synchrotron sources with high brilliance and coherence together with the development of better high-resolution fast-readout detectors giving high signal to noise ratio.

To directly apply the reconstruction algorithms of X-ray tomography on the SAXS signal the scattering particles must either be spherically symmetric or only the signal along the rotation axis can be used [2, 3]. This has been done in earlier work [4]. These limitations set a lot of constraints to which material systems the reconstruction algorithms can be used on. Reconstructing the cross section of a sample beyond these constraints has been attempted before on talc infused isotactic polypropylene by using a method of linear equations in the MSc thesis of E. T. B. Skjønsfjell [2].

1.3 Computational Optical Microscopy

As stated above, the design of the light microscope has arguably changed little during the past centuries much due to the fundamental physical limitations. Various designs have arisen to overcome certain difficulties of the visible optics, like chromatic aberrations, and there has been a lot of research over the years to improve the hardware of the optical systems, notably the lenses. The most radical improvements in recent years is the work done by various research groups to make the optics smaller, and improve image properties through computational imaging[1] [2]. This is made possible by the revolution of computers giving cheap computation power, and the development of better and smaller high resolution detectors. Together with new computer algorithms this has opened up new doors for all types

[1] See for example work done by the Laura Waller research group: http://www.laurawaller.com/

[2] See work done by the Aydogan Ozcan reasearch group: http://innovate.ee.ucla.edu/welcome.html

of imaging. One of the more notable developments in the area of light microscopes is in the work done by Zheng et. al. with digital refocusing and Fourier Ptychography [5, 6]. In these setups the traditional back light of the microscope is replaced with an LED array giving the possibility of illuminating the sample from different angles on the same experimental setup, named in this thesis Varied Illumination Microscopy (VIM).

1.4 The two Objectives of this Thesis

With traditional texture methods, an average orientation distribution function is obtained. If different orientations are observed, it is still not known how the different orientations relate to different spatial positions within the sample. Developing a technique capable of retrieving the three-dimensional orientation distribution of particles inside a sample, would be of great interest for industry and science alike. Retrieving spatially resolved orientations is one of the key objectives of this thesis.

In the work done by Skjønsfjell to reconstruct the three dimensional orientation of talc particles from scattering normal to the rotation axis, two methods were attempted [2]. The method of linear set of equations gave promising results, but with a lot of image artifacts as the complexity of the reconstruction increased. The method of simulated annealing was attempted but found unsuccessful in retrieving the distribution, and would require a more thorough investigation. In the present thesis the method of SA is revisited to analyse in greater depth if the SA method of minimizing a cost function could be able to retrieve the orientation distribution from SAXS tomography data. The orientation distribution of the talc particles has earlier been measured with other methods, on a physically cut sample [7]. This made it also possible to investigate if constraints of slowly varying structural gradients imposed on the system could be used to improve the results.

To make this method work would not only be useful for polypropylene but for other samples where the scattering particles are sufficiently monodisperse and monomorphous as well. Nano and microscale particles can be added to a sample to improve the physical properties e.g. mechanical, elextrical or optical. For example, if such a particle has anisotropic properties

the manufacturing process could be tailored to give the sample predefined properties in each direction in terms of orientation distribution of the particles. To map the orientation distribution the sample normally has to be cut to do measurements on a smaller sub-sample with the same properties. However, cutting the sample may alter the properties of the sample, and thus not give a correct image of how the particles are oriented in the uncut sample. A method for investigating the particles in uncut samples would not only remove the risk of altering the properties during cutting, but also make the sample eligible for *in situ* experiments. This would make it possible to see how the particles reorganise under mechanical loading.

The second objective of this thesis was to make a VIM that is capable of conventional bright- and dark-field imaging, and to use exposures made at different illumination-angles to re-focus the images *after* the measurements. Further use of the microscope shall hopefully make it capable of demonstrating *Fourier ptychography*.

Ptychography is a method dedicated to solving the phase problem for intensity measurements. Small areas of the sample are illuminated consecutively, and each measurement overlaps with the measurement of adjacent areas. Ptychography is increasingly used with X-ray and electron microscopes, and has also been shown to work with optical microscopes [8, 9] In the adaption made by Zheng for optical light, overlapping regions were made in Fourier space instead of real space, thereby the name Fourier ptychography. By using reconstruction algorithms it is possible to retrieve the phase field together with a microscope image of higher resolution.

X-ray ptychography is a highly complicated technique and a hot topic in current research [10, 11]. Performing experiments requires coherent beams with high brightness and are usually carried at a synchrotron. For these reasons a light based microscope capable of demonstrating ptychography is of great interest. By developing our own adaptation of the VIM we will be able to demonstrate and further develop complicated computational imaging techniques using only a small, cheap and harmless visible light microscope. The VIM is also intended to be used as an educational tool for new students to familiarise them with currently existing techniques and algorithms used in research. This could make it possible to discover new and exciting techniques in both X-ray imaging and visible light microscopy.

1.5 Structure of Thesis

This thesis is made up of two parts, one for each sub-project. Each part is made up of four chapters. Even though the projects are related to the same work, splitting them into two parts lets the key elements of each projects come through clearly, and creates a better reader experience.

In Part I SAXS tomography is presented. In the theory chapter the basic principles of SAXS tomography are described, then the principles of CT and simulated annealing are explained. In the Procedures and Experiments chapter the iPP sample and who the experimental data were gathered will be presented. Simulating the scattering signal is described together with how the orientation distribution is retrieved. The next chapter is Results from SAXS tomography. The part ends with a Discussion chapter going through the experimental results and methods.

In Part II VIM is presented. The theory chapter starts off with explaining the basic principles of optics and microscopy and finishes off with optical instrumentation and how the VIM can be used for refocusing. In the Experiments and Procedures chapter a walkthrough of the hardware used on the microscope is included, followed by an explanation of the software developed. At the end of the chapter imaging using the VIM is explained. Part II ends with a discussion of the capabilities of the VIM and the results obtained.

In the last chapter of the thesis conclusions for both projects are drawn.

Part I

Small-Angle X-ray Scattering Tomography

Chapter 2

SAXS Tomography Theory

2.1 Geometry of SAXS Tomography

For the SAXS tomography three coordinate systems are used as can be seen graphically in Figure 2.1; The laboratory frame, the sample frame and the talc particle frame. They all share one axis which is the z-direction which is also the rotation axis used in the tomography experiments. Note that this z-axis also coincides with the long axis of the polymer dog bone studied, and thus with the injection molding direction.

The (θ,y)-coordinates is the fixed laboratory frame. Positions inside the iPP sample are represented by the (s,t)-coordinates, where s is the direction of the long edge of the rectangular iPP sample, and t is the direction of the short edge. When the sample is rotated during the tomography procedure the sample system is related to the laboratory system by an angle Ω between the θ-axis of the laboratory and the s-axis of the sample. The last coordinate system is the frame of the talc particles, denoted by (x',y')-coordinates. How these coordinates are related to the talc particles can be seen in Figure 2.1. The talc frame says how the talc particles are oriented inside the sample by an angle ϕ between the s-axis of the sample frame and x-axis of the talc frame. The talc frame is related to the laboratory frame by the angle $\psi = \phi + \Omega$.

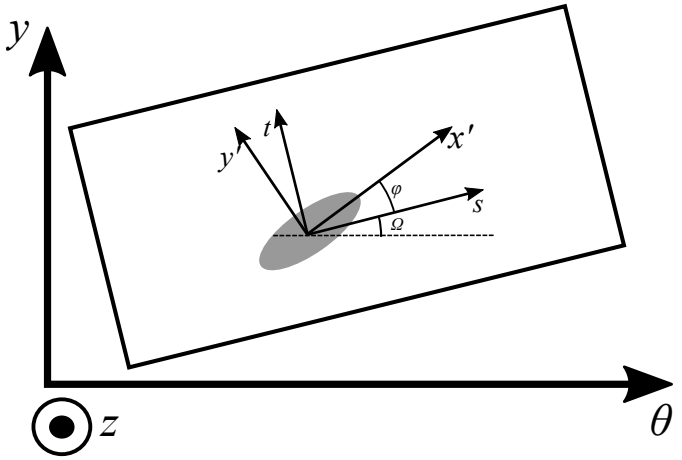

Figure 2.1: Overview of the required coordinate systems needed to describe the geometry of the SAXS tomography. (θ, y) is the lab frame. (s, t) is the sample frame, and (x', y') is the talc particle frame. The z-axis of all three systems are parallel and go out of the paper.

2.2 Electromagnetic Waves and Scattering Theory

There are two different ways of regarding electromagnetic radiation. Either as a quantised stream of photons or as waves. The photons are described by their energy $E = hf$, where h is Planck's constant and f is the frequency. This view of the electromagnetic radiation is well suited when the energy of the incoming and scattered photon is of interest, such as Compton scattering and various methods of spectroscopy. In the wave formalism the radiation is regarded as waves propagating in agreement with Maxwell's equations. The polarisation is perpendicular to the direction of propagation. The latter description is the one that will be used for describing the work done in this thesis regarding X-ray scattering.

In the X-ray regime materials have a refractive index slightly less that unity. Although a perfect collimation of light is not possible, a plane wave approximation of the X-rays is usually valid since the radius of curvature is much larger than the width of the beam hitting the sample. Thus the electric field of the incoming X-ray beam can be written as a plane wave, to be consistent with the notation presented in the previous section, propagating in the

y-direction and polarised in the z-direction,

$$\boldsymbol{E}(y,t) = \hat{\boldsymbol{z}} E_0 e^{i(k_y y - \omega t)}. \tag{2.1}$$

Here $\boldsymbol{k} = \frac{2\pi}{\lambda}\hat{\boldsymbol{k}}$ is the wave vector giving the direction of propagation, $\hat{\boldsymbol{z}}$ is the polarisation vector, and ω is the angular frequency of the wave [12].

2.2.1 Scattering From a Single Particle

When the electromagnetic wave of Equation (2.1) hits the sample, it will start acting with a force on the charged particles that will be accelerated and thus begin to radiate. Considering only a single particle, the radiated power dP into a small solid angle $d\Omega$ is given by [13]

$$\frac{dP}{d\Omega} = \frac{q^2}{4\pi^2\epsilon} \frac{|\hat{\boldsymbol{r}} \times (\boldsymbol{u} \times \boldsymbol{a})|^2}{(\hat{\boldsymbol{r}} \cdot \boldsymbol{u})} \tag{2.2}$$

where q is the electrical charge of the particle, $\hat{\boldsymbol{r}}$ is the unit vector in the radial direction, and ϵ is the electric permittivity of the sample, and $\boldsymbol{a}$ is the acceleration of the electron. $\boldsymbol{u} = c\hat{\boldsymbol{r}} - \boldsymbol{v}$ where c is the speed of light and $\boldsymbol{v}$ is the velocity of the electron.

Assuming the particle to be situated at $y = 0$ and that the electric field of the incoming electromagnetic wave is in the form of Equation (2.1), solving the equations of motion gives acceleration and velocity

$$\boldsymbol{a} = \frac{eE_0}{m} \sin(\omega t)\hat{\boldsymbol{z}} \tag{2.3}$$

$$\boldsymbol{v} = \frac{eE_0}{m\omega} \cos(\omega t + \alpha)\hat{\boldsymbol{z}} \tag{2.4}$$

Putting Equation (2.3) and Equation (2.4) into Equation (2.2) we get the radiated power per solid angle

$$\frac{dP}{d\Omega} = \frac{e^4 E_0^4}{16\pi^2\epsilon m^2 c^3} \frac{\sin^2(\omega t_r)\sin^2(\theta)}{(1 - \frac{eE_0}{m\omega c}\cos(\theta)\cos(\omega t_r + \alpha))^5} \tag{2.5}$$

Here $t_r = t - r/c$ is the retarded time taking into account the time required

for the radiation to travel the distance r, and θ is the angle formed by the radial unit with the wave vector of the incoming wave, in this case the z-axis. Note that the radiated power depends on $1/m^2$, which means that lighter particles will radiate more than heavy particles. For this reason only the electrons are taken into consideration in X-ray scattering, since the protons are several orders of magnitude heavier than electrons and thus will radiate less.

2.2.2 Scattering From Several Charged Particles

Looking at the scattering from several electrons in an atom, it will be convenient to instead use an electron number density distribution $\rho(\boldsymbol{r})$. The total scattered radiation is then a superposition of the contribution from all the volume elements in the distribution. Depending on their phase differences these will interact to create interference patterns. The scattered intensity from a single atom is given by its atomic form factor which is the Fourier transform of the electron number density

$$f^0(\boldsymbol{Q}) = \int \rho(\boldsymbol{r}) e^{i\boldsymbol{Q}\cdot\boldsymbol{r}} d\boldsymbol{r} \tag{2.6}$$

$\boldsymbol{Q} = \boldsymbol{k_f} - \boldsymbol{k_i}$ is the scattering vector which is the difference between the wave vector of the incoming k_i and outgoing k_f wave. $\boldsymbol{r}$ is the position vector of the volume elements. The scattering angle 2θ is the angle between the incoming and scattered wave.

Widening the reach further and taking into account several atoms in a molecule the total scattering is the sum of the atomic form factor $f_j(\boldsymbol{Q})$ of the j'th atom in the molecule with an added phase factor $e^{i\boldsymbol{Q}\cdot\boldsymbol{r_j}}$.

$$F(\boldsymbol{Q}) = \sum_j f_j(\boldsymbol{Q}) e^{i\boldsymbol{Q}\cdot\boldsymbol{r_j}} \tag{2.7}$$

The scattered intensity from a single atom is given by the absolute square of the atomic form factor, the same goes for a molecule where the scattered intensity is proportional to the absolute square of the molecular form factor [13]. Taking this into account and assuming all scattering atoms to be identical the scattered intensity from a molecule can be written.

$$I(\boldsymbol{Q}) = |f(\boldsymbol{Q})|^2 \sum_n e^{i\boldsymbol{Q}\cdot\boldsymbol{r}_n} \sum_m e^{i\boldsymbol{Q}\cdot\boldsymbol{r}_m} = |f(\boldsymbol{Q})|^2 \sum_n \sum_m e^{i\boldsymbol{Q}\cdot(\boldsymbol{r}_n - \boldsymbol{r}_m)} \tag{2.8}$$

Proceeding with separating the summation over $n = m$ and $n \neq m$, and substituting the summation over m with an integral over the average atom density ρ_{at} in the volume V, the scattered intensity takes the form

$$\begin{aligned} I(\boldsymbol{Q}) =& N|f(\boldsymbol{Q})|^2 + |f(\boldsymbol{Q})|^2 \sum_n \int_V [\rho_n(\boldsymbol{r}_{nm}) - \rho_{at}] e^{i\boldsymbol{Q}\cdot(\boldsymbol{r}_n - \boldsymbol{r}_m)} dV_m \\ &+ |f(\boldsymbol{Q})|\rho_{at} \sum_n \int_V e^{i\boldsymbol{Q}\cdot(\boldsymbol{r}_n - \boldsymbol{r}_m)} dV_m \end{aligned} \tag{2.9}$$

where $\rho_n(\boldsymbol{r}_{nm})$ is the number density at the relative position $\boldsymbol{r}_n - \boldsymbol{r}_m$. When the sample is not crystalline, the density at position $\boldsymbol{r}_{nm}$ will quickly approach the average density ρ_{at} and the second term in Equation (2.9) will therefore vanish for large $\boldsymbol{r}_{nm}$ [13]. The third term on the other hand will only contribute for small scattering vectors $\boldsymbol{Q}$. This is because the phase factor will oscillate quickly and will add up to zero unless $|\boldsymbol{Q}|$ is small. Low $|\boldsymbol{Q}|$-values means large distances in real space and small scattering angles 2θ. Hence, this term is called the small angle X-ray scattering signal (SAXS) and is sensitive to fluctuations of the average electron density at the meso-scale.

2.2.3 Small-Angle X-ray Scattering

As is understood SAXS considers the scattering at small angles, which makes it possible to do analysis through a number of simplifications. If the atomic form factor $f(\boldsymbol{Q})$ varies little for small Q, the SAXS term of Equation (2.9) can be written

$$I^{SAXS}(Q) = |f|^2 \sum_n \int_V \rho_{at} e^{i\boldsymbol{Q}\cdot(\boldsymbol{r}_n - \boldsymbol{r}_m)} dV_m = |f|^2 \sum_n e^{i\boldsymbol{Q}\cdot\boldsymbol{r}_n} \int_V \rho_{at} e^{-i\boldsymbol{Q}\cdot\boldsymbol{r}_m} dV_m \tag{2.10}$$

Doing the same transformation as in Equation (2.9) by changing from a sum to an integral, this becomes

$$I^{SAXS}(Q) = |f|^2 \int_V \rho_{at} e^{i\boldsymbol{Q}\cdot\boldsymbol{r}_n} dV_n \int_V \rho_{at} e^{-i\boldsymbol{Q}\cdot\boldsymbol{r}_m} dV_m \tag{2.11}$$

When averaged this becomes [13]

$$I^{SAXS}(Q) = |\int_V \rho_{sl} e^{i\boldsymbol{Q}\cdot\boldsymbol{r}} dV|^2 \tag{2.12}$$

where $\rho_{sl} = f\rho_{at}$ is called the scattering length density. The integral would generally have to be taken over the whole volume of the sample. However, if considering a dilute solution of identical particles, there will be no constructive or destructive interference due to ordering, and the scattered intensity is then the absolute square of the difference between the scattering length density of the particle and the solvent [12]. If the scattering length density of each particle $\rho_{sl,p}$ is uniform, and the same for the solution $\rho_{sl,0}$ the scattering intensity for a single particle becomes

$$I_1^{SAXS}(Q) = (\rho_{sl,p} - \rho_{sl,0})^2 \int_{V_p} |e^{i\boldsymbol{Q}\cdot\boldsymbol{r}} dV_p|^2, \tag{2.13}$$

where V_p is the volume of the particle. If the integral is changed from the whole sample to only consider one particle, the single particle scattering intensity has to depend on the difference between the scattering length density of the particle and solvent. If they had the same scattering length one would not be able to differentiate between the particle and solvent in the scattering data. Introducing the single particle form factor

$$F(\boldsymbol{Q}) = \frac{1}{V_p} \int_{V_p} e^{i\boldsymbol{Q}\cdot\boldsymbol{r}}, \tag{2.14}$$

which is the Fourier transform of the particle shape, Equation (2.13) becomes

$$I_1^{SAXS}(\boldsymbol{Q}) = \Delta\rho^2 V_p^2 |F(\boldsymbol{Q})|^2, \tag{2.15}$$

where $\Delta\rho = (\rho_{sl,p} - \rho_{sl,0})$.

2.2.4 Porod Exponent

The Porod regime is in the short wavelength limit of the SAXS regime, when Q gets relatively large compared to the particle size R^{-1}, but is still too small compared to inter-atomic spacing, i.e. $QR \gg 1$. In this region the scattered intensity is dependant on the shape of the surface of the particles. When calculating the particle form factor for simple shapes such as a rod, disk or a sphere the scattered intensity will exhibit characteristic power dependence $I \propto Q^n$ based on the dimensionality of the particle. This exponent n is called the Porod exponent. To analytically calculate this Porod exponent can only be done for a few highly symmetric particle shapes, more complex shapes will require numerical integration methods. The shapes mentioned above can be analytically calculated, where the rod with dimension 1, has Porod exponent $n = -1$, whereas the disc with dimensionality 2, and sphere with dimensionality 3 have Porod exponents -2 and -4 respectively[13]. Figure 2.2 shows how the dominating feature of the form factor of the talc particles can be changed by multiplying it with a Q^r factor.

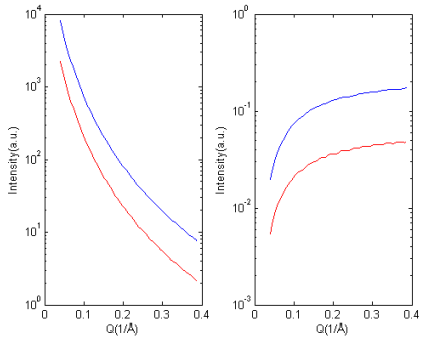

Figure 2.2: The theoretical scattering intensity of the talc particles as a function of Q at two different orientations of the particles 90° apart. a) The theoretical scattering intensities. b) The same scattering patterns multiplied with a factor Q^4.

2.2.5 Polydispersivity

When the particles analysed are all of the same size the system is called monodisperse. On the other hand, if the particles are no longer of the same size, but are taken from a size distribution $D(\boldsymbol{R})$, they are polydisperse. To

take into account the variations of the particle size the scattering intensity of Equation (2.15) has to be modified to

$$I(\boldsymbol{Q}) = \Delta\rho^2 \int_0^\infty V_p^2(\boldsymbol{R})|F(\boldsymbol{Q},\boldsymbol{R})|^2 D(\boldsymbol{R})d\boldsymbol{R}, \tag{2.16}$$

where $D(\boldsymbol{R})$ is normalised such that

$$\int_0^\infty D(\boldsymbol{R})d\boldsymbol{R} = 1. \tag{2.17}$$

Polydispersivity causes features of the SAXS signal to be smeared out and become less distinguishable.

2.3 Form Factor of the Talc Particles

In order for the simulated annealing method to work, a good model of the form factor of the talc particles is needed. It is known that in talc reenforced polypropylene the talc particles have the shape of thin flakes with their surface normal orthogonal to the z-axis [7]. It has also previously been shown that modelling these flakes as oblate ellipsoids gives good fits to experimental data [2].

The scattering form factor of an ellipsoid F_{elli} is given by:

$$F_{elli}(\boldsymbol{Q'},R,H) = e^{\frac{iQ_{y'}H}{2}} \int_0^{H/2} 4\pi R_{y'}^2 \frac{J_1(Q_{||'}R_{y'})}{Q_{||'}R_{y'}} \cos(Q_{y'}y')dy' \tag{2.18}$$

Here $J_1(x)$ is the Bessel function of first order. The other variables are given by

$$\begin{aligned} Q_{||1} &= \sqrt{Q_{x'}^2 + Q_{y'}^2} \\ R_{y'} &= R\sqrt{1 - 4\frac{y'^2}{H^2}} \end{aligned} \tag{2.19}$$

and the R and H dimensions are indicated in Figure 2.3

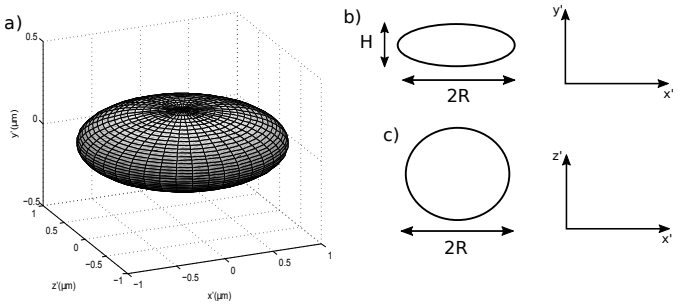

Figure 2.3: a) Illustration of the ellipsoide shape assumed for the talc particles. b) The dimensions of the ellipsoide and how they relate to the coordinate systems.

2.4 Absorption

When and X-ray beam propagates through a material the intensity of the beam is attenuated due to photoelectric absorption. How much the beam is attenuated is given by the linear absorption coefficient μ of the specific material, and the intensity I of the beam after travelling a distance l through the material is given by

$$I = I_0 e^{-\int_l \mu(s,t,z)dl}. \tag{2.20}$$

This is a line integral over a distance l through the sample, I_0 is the initial intensity and $\mu(s,t,z)$ is the attenuation coefficient which in general is spatially varying throughout the sample and energy dependent. However, the experimental data which this report builds on were done with a monochromatic beam at the Swiss Light Source and energy dependent effects ,including beam hardening, are not relevant in this case. To faithfully model the experimental data it is required that Equation (2.20) is accounted for.

In general the attenuation coefficient is small for soft materials such as polymers and tissue making the corrections small compared to the signal intensity. It is however important when the distance the beam travels through the sample varies significantly with the sample orientation [14].

2.5 Computational Tomography

Computational tomography (CT) is a method to create a cross-section image of the interior of a sample. The method is based on taking several projection images at different angles. It is then possible to reconstruct the three-dimensional distribution of a given variable throughout the sample, as long as the information can be found in the projections.

CT is often used in medicine to find the distribution of the absorption coefficient $\mu(\vec{r}))$ in the human body. Traditional absorption contrast will be used here to give a conceptual explanation of how CT works. When an X-ray travels through a sample the direct beam will be attenuated in accordance with Equation (2.20). This equation can be made into

$$p(\theta, \Omega) = \ln(\frac{I_0}{I}) = \int_y \mu(s,t)dy, \tag{2.21}$$

which is a projection of the attenuation coefficient along the beam path y. $p(\theta, \Omega)$ is the Radon transform of the attenuation coefficient μ at angle Ω. Doing these projections at many positions θ gives the so-called projection profile. How these projection profiles vary with the angle is illustrated in Figure 2.4, where the dark regions have high attenuation, and the rest of the sample has low attenuation.

After getting the projection profiles at different values of Ω, the task is to reconstruct $\mu(s,t)$. This is often done by doing the two dimensional Fourier transform and utilising the Fourier slice theorem. The two dimensional Fourier transform of the function $\mu(s,t)$ is defined as:

$$F(\nu_\theta, \nu_y) = \int_{-\infty}^{\infty}\int_{-\infty}^{\infty} \mu(s,t)e^{-2\pi i(\nu_y y + \nu_\theta \theta)}dyd\theta. \tag{2.22}$$

Here the integrals have been taken over θ and y tilted with respect to the sample frame. Setting ν_y = 0 is the same as looking at the Fourier transform along the θ-axis. The integral then becomes

$$F(\nu_\theta, 0) = \int_{-\infty}^{\infty} e^{-2\pi i(\nu_\theta \theta)} \int_{-\infty}^{\infty} \mu(s,t)dyd\theta \tag{2.23}$$

The innermost integral can now be substituted with Equation (2.21) to ob-

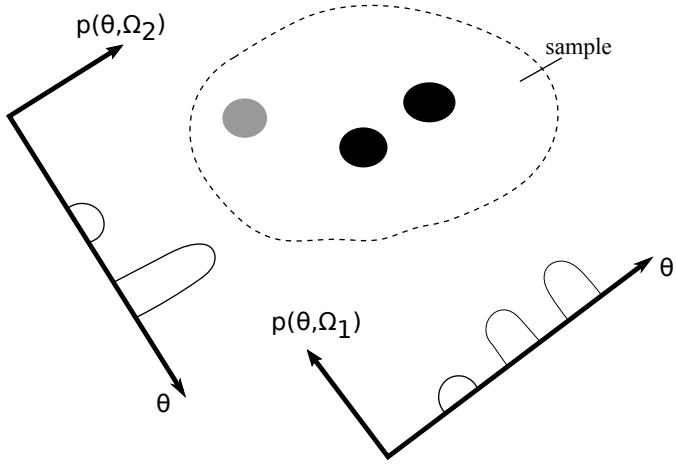

Figure 2.4: The Radon transform of a sample at two different rotation angles Ω. The black regions in the sample are regions of high attenuation, grey regions have low attenuation, while the rest of the sample does not attenuate. Projecting them on to the line will create different projection profiles base on the direction they are projected.

tain

$$F(\nu_\theta, 0) = \int_\theta p(\theta, \Omega) e^{-2\pi\nu_\theta} d\theta = P(\nu_\theta, \Omega) \tag{2.24}$$

This means that the Fourier transform of the projections $p(\theta, \Omega)$ is the same as the Fourier transform of $\mu(s, t)$ projected onto a line at angle Ω with the s-axis. The most intuitive way of solving this would be to take the direct inverse Fourier transform. However, a direct inverse Fourier transform would require continuous dataset, i.e. infinitely many angles, with infinitely small step lengths. When doing measurements, no matter how good the resolution of the data is, there will be a finite number of measurement points. There are a number of different ways to get around this, such as filtered backprojections. The work done in this thesis goes around the problem of the inverse Fourier transform by simulating the scattering pattern of a theoretical sample and comparing with the experimental data through the use of simulated annealing. A good match between the theoretical and experimental data will then mean the configuration of the theoretical sample is close to the real sample.

2.6 Simulated Annealing

Simulated annealing (SA) is a numerical method for minimising functions. It has proven well suited for problems of large scales, and having many control parameters, where the global minimum is difficult to find among many poorer local minima. SA a random search algorithm which exploits the analogy of how a material undergoes a phase transition when it is cooled in search for the global minimum energy. With this easy chain of thought SA can be applied to many minimisation problems, by defining the energy function E, a temperature T and an annealing schedule for the system. Performing Monte-Carlo steps to explore the different configurations given by the Boltzmann probability distribution

$$p_i \propto e^{-E_i/T} \tag{2.25}$$

In each step of the Monte-Carlo algorithm the system will be in an energy state E_i and the probability of being in that state is p_i. It will then attempt to move to an energy state E_j which has probability p_j. Whether the step should be completed or not is given by whether the ratio p_j/p_i is larger than a random number between 0 and 1. If this criterion is not met the system will stay in the original state. That little detail of a random number is what gives SA one of its greatest strengths. A pure random search algorithm only checks if the energy of the new state is lower than of the initial state, i.e. check if the probability ratio is greater than one. By instead comparing it to a random number, the system is able to do an unfavourable step by increasing its energy. This makes it able to escape local minima. The second good feature is that the whole probability distribution does not need to be known, only their ratios.

The algorithm starts by defining the initial temperature T and an annealing procedure of the system. It will then perform a cycle by attempting to do a set amount of Monte-Carlo steps. After the cycle is complete, if the energy of the system is lower than before the cycle started, the temperature is decreased $T \rightarrow T'$ in accordance with the annealing procedure. A new cycle of Monte-Carlo steps is then performed. These steps are repeated until the minimum is reached.

This algorithm is easy to implement on a computer, however there can be great challenges regarding finding a good starting temperature, and an annealing schedule that is "sufficiently slow" to get close to the global minimum without being too slow.

In many cases certain properties of the sample may be already known, such as slowly spatially varying parameters of preferred orientations. Instead of searching through the system completely at random, and possibly ending in an undesired local minimum, constraints can be applied to the system. These constraints may be incorporated in the energy function by making it prefer steps that coincide with the known properties of the sample. In this way prior information can be provided to the system. Easy as it may be to apply, these constraints require a good model to influence the system in the desired manner. The idea of imposing constraints on the system is to improve the results that can be obtained without them to increase convergence rate and stability of the results. If the energy function depend too heavily on the constraints, they will dominate the decisions made by the algorithm and possibly give erroneous results. If the constraints are too weakly imposed the results will not depend on them at all.

Chapter 3

SAXS Tomography Procedures and Experiments

3.1 The Sample Analysed

The sample chosen to generate the experimental data used in this thesis was injection molded talc reinforced isotactic polypropylene (iPP), kindly provided by SINTEF. The shape of the sample resembles a dog bone that can be seen in Figure 3.1. The injection molding was done parallel to the axis of the long dog bone neck under low temperature and shear rate. The reason for reinforcing polypropylene with talc is to improve the mechanical properties of the polymer [7]. Talc is a mineral with chemical formula $H_2Mg_3(SiO_3)_4$ that crystallises in a monoclinic unit cell. For X-rays with wavelength 1Å talc has an absorption coefficient $\mu = 23.1$ cm^{-1}. Polypropylene on the other hand consist of long chains of hydrocarbons with some hydrogen atoms replaced with CH_3. It has an absorption coefficient of $\mu = 0.94$ cm^{-1} for X-rays of wavelength 1Å [2]. Since talc consists of inorganic heavier elements than polypropylene the scattering length density of the talc particles will be a lot higher than that of polypropylene. The SAXS scattering intensity in Equation (2.15) will then to a high degree be dominated by the talc particles.

The size and shape of the talc particles have earlier been measured using Scanning Electron Microscopy(SEM) to make up thin flakes. In addition it has been shown using raster scanning SAXS on a cut sample that the

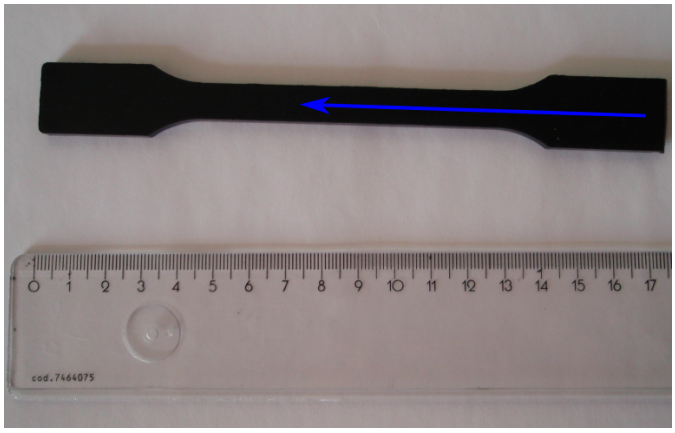

Figure 3.1: The sample used in the SAXS tomography experiments. The resemblance to a dog bone can clearly be seen. The blue arrow indicates the direction of injection during molding. The ruler is added for size comparison.

particles have a preferred orientation with their surface normals orthogonal to the outer edges of the sample. This meant that retrieving the three dimensional orientation distribution of the talc particles on a cross section normal to the long dog bone neck of the sample could be simplified to a two-dimensional problem. This knowledge, and the large difference in scattering lengths in the sample made iPP well suited for the SAXS tomography experiments. The results of the raster scanning SAXS can be seen in Figure 3.2. With the orientation distribution already known, this could be used as a benchmark for the results obtained with SAXS tomography.

3.2 Gathering Experimental Data

The experimental SAXS tomography data were gathered at the cSAXS beam line at the Swiss Light Source(SLS) at the Paul Scherrer Institute in Switzerland. The SLS is a third generation synchrotron and the cSAXS beam line is specialised for small-angle X-ray scattering. A schematic of the X-ray optics setup can be seen in Figure 3.3.

The diamond filter separates the vacuum of the synchrotron and the beam line. The slits control the shape of the beam. The monochromator works by letting the beam hit a Si crystal, and only the wavelengths fulfilling the

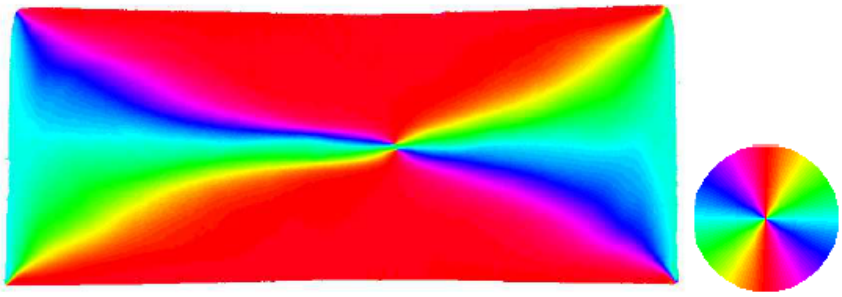

Figure 3.2: The orientation distribution of the talc particles surface normal previously obtained using raster scanning SAXS. This is a cross sections normal to the long neck of the dog bone iPP sample, that was physically cut to do the experiments. Figure adopted from [2].

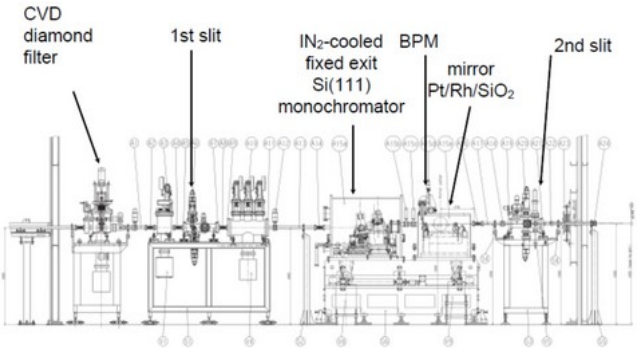

Figure 3.3: Setup of the X-ray optics before entering the sample. Image taken from the SLS website[1].

Bragg diffraction condition of the (111) direction the crystal are able to pass through. By changing the angle of the crystal different wavelengths can be chosen. The mirror is position close to the critical angle of internal reflection. This way higher harmonics of the incoming beam will be refracted into the mirror while lower frequencies will be reflected and hit the sample. After the X-ray optics the sample is placed in such a way that the beam will hit the neck of the dog bone sample. The X-rays were being collected by a 7 m long flight tube after scattering from the sample before hitting the detector. Flight tubes are usually evacuated or filled with a light gas and are often used in X-ray experiments to minimise undesired back-

[1] Image on SLS website http://www.psi.ch/sls/csaxs/beamline-layout

ground scattering along the beam path. The total sample-detector distance was 7.2 m. The 2M PILATUS detector consist of 1475x1679 pixels of size 172x172 μm^2 that captures the scattering data

This method of SAXS tomography, however, is only concerned with the scattering pattern in the Q_θ-direction, meaning that the complete dataset contains a lot of unused information. The data recorded by the detector was sectioned into 16 different sectors, each of which were azimuthally averaged creating 1-dimensional scattering patterns $I(Q)$. The sectioning of the detector area is illustrated in Figure 3.4. The four regions containing the horizontal scattering pattern were summed to get the total scattering data for this position of the SAXS tomography scan. This procedure was applied to all measured combinations of θ and Ω to give the complete 3-dimensional experimental data set $I(Q, \Omega, \theta)$, called a sinogram.

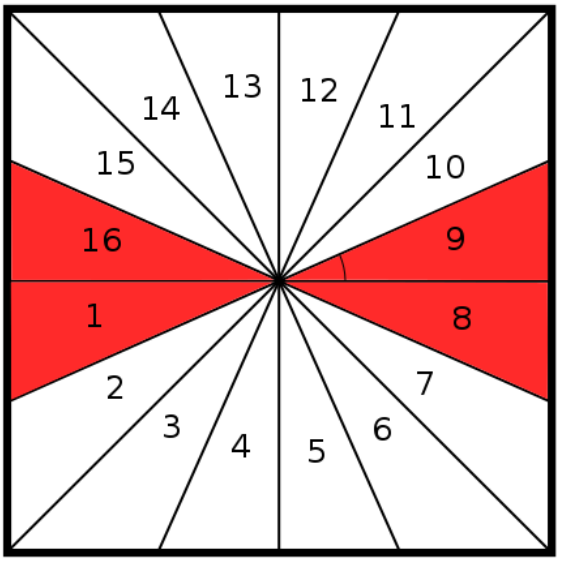

Figure 3.4: The sectioning of the detector area into 16 different regions. The red areas denote the regions that contain the equatorial scattering used in the subsequent analysis. The tangential line in sector 9 shows the direction the intensities of each region were integrated up and averaged.

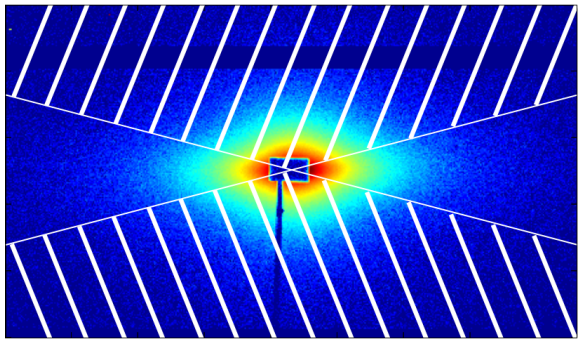

Figure 3.5: Experimental 2D scattering pattern from the SAXS tomography measurements. The unshaded area is the horizontal scattering signal. The rectangular beam stop in the centre contained a diode.

3.3 Simulating SAXS Tomography

The talc particles were assumed to be oblate ellipsoids, as explained in Section (2.3), with average dimensions R =3μm H =2.25 μm. The particle density was assumed to be uniform throughout the sample. Equation (2.15) states that the scattering intensity is proportional with the absolute square of the scattering form factor. The tomographic scan was then simulated by calculating the distance an X-ray beam travels through the regions of the sample of particles of different orientation and multiplied with the absolute square of the scattering form factor for that given orientation. This was done in a line scan at different positions θ, and at different rotation angles Ω of the sample as illustrated in Figure 3.6.

In practice this was done by creating a theoretical sample of the same shape as the real sample. The theoretical sample used when retrieving the orientation distributions contained 2851 regions and can be seen in Figure 3.7. The horizontal scattering pattern $I(Q, \phi, \Omega)$ of an individual particle was calculated for all experimentally measured projection angles of the tomographic scan. n possible particle orientations ϕ_n were selected to be used to retrieve the orientation distribution. From previous measurements of the orientation distribution it was known that the spatial gradient of the distribution is low, then each region of the theoretical sample could be assumed to contain particles of only one orientation. n matrices of the theoretical sample were made, each corresponding to one of the possible particle orientations. If

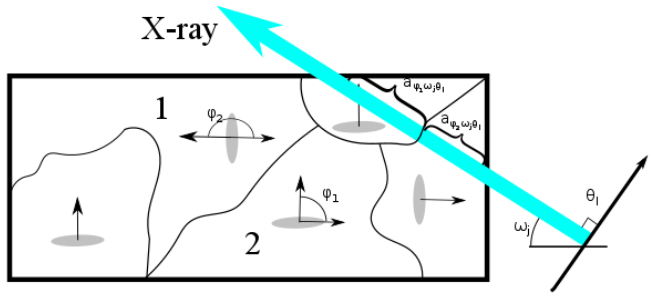

Figure 3.6: A cross section of the sample. For each rotation angle Ω_j the X-rays at position θ_l of the linescan travel a distance $a_{\phi_i,\Omega_j,\theta_l}$ through the regions of the sample containing talc particles (grey ellipses) of different orientations ϕ_i

a region of the currently retrieved orientation distribution had orientation ϕ_i, that region of matrix i would have the value 1, and 0 otherwise. The distance $a_{\phi_i,\Omega_j,\theta_l}$ the X-ray beam travelled through regions of different orientation ϕ_i at position (θ, Ω) of the tomographic scan, were calculated by taken the radon transform of the n matrices individually and scaled so that the total distance $d_{\Omega,\theta} = \sum_i a_{\phi_i,\Omega_j,\theta_l}$ through the theoretical sample coincided with distances through the real sample. At position θ_l and rotation angle Ω_j of the tomographic scan the scattered intensity was calculated by

$$I(Q, \Omega_j, \theta_l) = \sum_{i=1}^{n} a_{\phi_i,\Omega_j,\theta_l} I(Q, \phi_i, \Omega_j) \tag{3.1}$$

By putting together these scattering data at all positions of the tomographic scan the complete 3-dimensional scattering dataset $I(Q, \theta, \Omega)$ was obtained.

The values of the Q-vectors when calculating the form factors were chosen to be the same as those measured experimentally, and the range used was Q = 0.0395 nm^{-1}-0.3902 nm^{-1}. These values are high enough that the experimental data were not affected by the beam stop, and low enough that the signal was not significantly influenced by inter-particle scattering in the sample. After simulating the scattering signal the sinograms had to be aligned to so that the projections of the experimental data and simulated data went through the same regions of the sample.

Figure 3.7: Image of the theoretical sample used for retrieving the orientation distribution. The red area is the sample, and the blue is air padding added around. It does not look like a smooth shape since this sample used only used 1/16 of the regions of the theoretical sample that was made. It consisted of 2851 regions, also called voxels.

3.3.1 Absorption

The model of the scattering form factor as given in Equation (2.18) does not include absorption. To account for this the simulations were modified in accordance with Equation (2.20). The absorption coefficient of talc reinforced iPP was assumed to be constant $\mu = 2.85$ cm^{-1} throughout the sample such that the absorption factor becomes $e^{d_{\Omega,\theta}\mu}$, where $d_{\Omega,\theta}$ equals the total distance travelled by X-rays through the sample at a given point (Ω, θ) in the tomography procedure.

3.4 Retrieving Orientation Distribution by Simulated Annealing

3.4.1 The Single Voxel Method

When simulating the scattering signal, calculating the radon transform is what consumes by far the most time, and it increases fast with increased size of the matrix to be transformed. Any simplification to this procedure may decrease the time required by the reconstruction algorithm tremendously.

When Matlab does the radon transform, it creates a line of bins for the line projections, it then split each index of the matrix to transform into four

equal regions. The values of the regions are projected on to the line and interpolated into the bins, and this is done for each index individually. This procedure is illustrated in Figure 3.8.

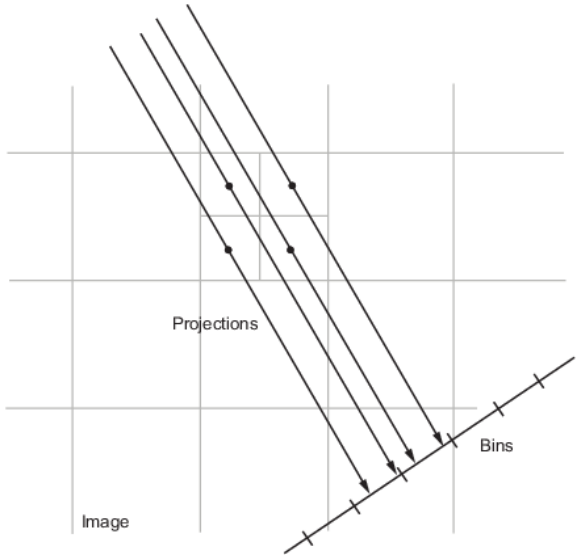

Figure 3.8: When Matlab does the Radon transform, each pixel is divided into four sub-pixels that are individually projected into the bins. Figure is adopted from the MathWorks homepage[1].

For each Monte-Carlo step in the algorithm only the orientation of a few voxels of the theoretical sample are changed before the scattering signal has to be simulated again to compare with the experimental data. This means that most of the simulated intensity will remain the same. This fact was utilised by instead of calculating the scattered intensity of the whole theoretical sample, an almost empty matrix containing only the regions of interest was used. The scattering signal of the voxels before and after the suggested Monte-Carlo step was calculated, and if the Monte-Carlo step was accepted, the single voxel scattering signals could simply be subtracted and added to the total scattering signal. This will in this thesis be called the single voxel method.

[1]Figure adopted from: http://se.mathworks.com/help/images/ref/radon.html

3.4.2 The Simulated Annealing Energy Function

To verify that the subjected function is able to retrieve the wanted orientation distribution, and its convergence rate, we made idealised numerical test cases. An SA energy function assuming no prior knowledge of the system is given by

$$E_0 = \frac{1}{N} \sum_{Q} \sum_{\Omega,\theta} (S_s(Q,\Omega,\theta) - S_t(Q,\Omega,\theta))^2 \tag{3.2}$$

Here S_s is the sinogram obtained by simulating horizontal scattering of the temporarily retrieved orientation distribution, and S_t is the one for the true orientation distribution obtained either from experimental SAXS tomography data or from simulated SAXS scattering from a synthetic orientation distribution. N is the number of voxels in the theoretical sample. The variables θ and Ω are the projections and the rotation angle during the tomography scan respectively. Q is the reciprocal scattering vector.

3.4.3 Constraints of Slow Spatial Variations on the Energy Function

Under the assumptions of slowly varying structural gradients, the energy function can be modified by adding a cost term ξD, giving

$$E = E_0 + \xi D. \tag{3.3}$$

Here ξ is assumed to be a system constant that had to be found, and D is a measure of how favourable the new orientation after the Monte-Carlo step is compared to the initial orientation. It was given an integer value based on how similar it was to the orientations in the nearest neighbour voxels. In Figure 3.9 scheme (a) will give a more favourable cost term ξD than the configuration in scheme (b).

This extra cost term will effectively smoothen the orientation distribution, making deviations in groups of voxels of the same orientation less favourable. It should again be emphasised that this can only be done with small structural gradients.

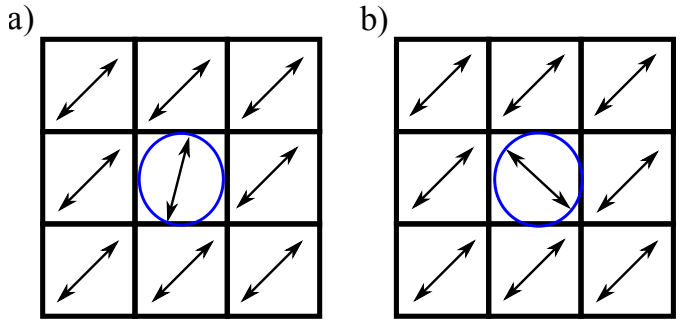

Figure 3.9: Two different possible outcomes of a Monte-Carlo step on the middle pixel. From this, scheme a) will give smaller D value than scheme b), thus a more favourable orientation

3.4.4 Increasing the Weight of High Q Measurements

The SAXS diminishes rapidly for increasing Q-values as described in Section (2.2.4). The way that the energy of the system is calculated in Equation (3.2) the total cost of the system will depend heavily on low Q-values while the scattering intensities for larger Q-values contribute very little to the total energy function. A Q^n-factor was multiplied into the scattering data to make the energy function depend more heavily on the scattering at higher Q.

$$E = \sum_{Q} \sum_{\Omega,\theta} ((S_s(Q,\Omega,\theta) - S_t(Q,\Omega,\theta))Q^n)^2 \tag{3.4}$$

Chapter 4

SAXS Tomography Results

4.1 Comparison of Theoretical Data

4.1.1 The Single Voxel Method

Because of the way MatLab performs the Radon transform, the single voxel method could be a simple, yet powerful way of reducing the runtime of the simulation by performing the radon transform of a matrix consisting of almost only zeros, rather than a matrix with nonzero values at every index. Two runtime tests of the radon transform in MatLab were performed. One run with every matrix index with value 1, and one run with all elements set to 0 except one that was set to 1. As can be seen from Figure 4.1, there is a significant reduction in the runtime of the Radon transform between the full and the single value matrices.

To ensure the single voxel method did in fact generate the same sinograms, the energies of the resulting simple method energy and the full method energy were compared using $|E_{full} - E_{single}|/E_{full}$. This ratio was in the range 10^{-15}-10^{-17} indicating small roundoff errors, however negligibly small. After confirming the correctness of the single voxel method, it was used for all simulations of SAXS tomography.

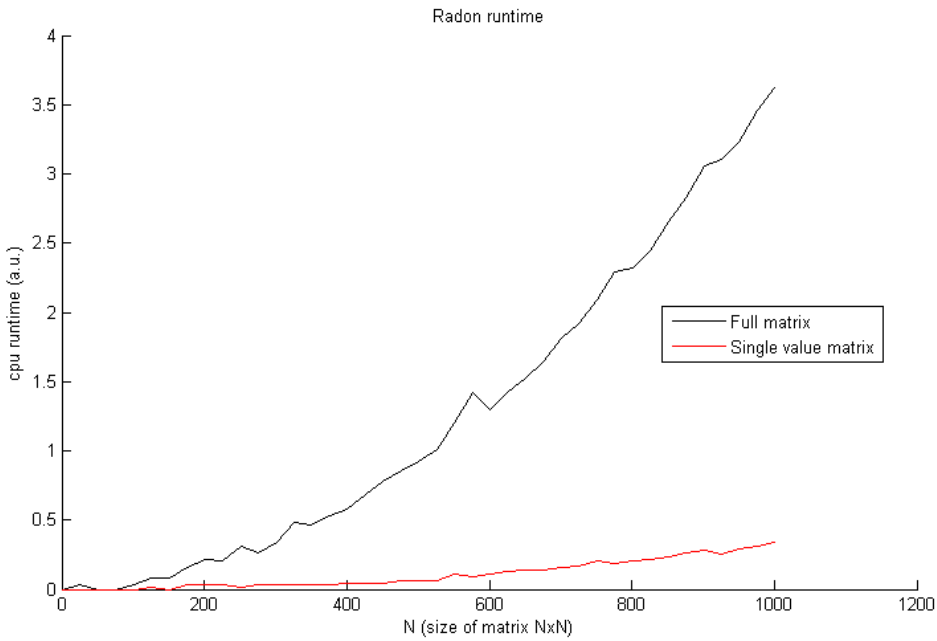

Figure 4.1: Plot of the CPU runtimes for full matrices (black) and matrices containing only one non zero value (red). The size of the matrices was from 1 to 1001 with increments of 25.

4.1.2 Retrieving Theoretical Orientation Distributions

Before working with experimental data, the algorithm with the unconstrained energy function of Equation (3.2) was tested to retrieve synthetic orientation distributions. The sinograms used to compare with the simulated SAXS data were achieved using the method described in Section 3.3.

Figure 4.2 shows the result of applying SAXS tomography orientation retrieval algorithm to a synthetic 10x10 system. The fact that the retrieved orientation is almost identical, indicates that minimising the energy function is indeed leading to retrieval of the orientation distribution. The black circle in Figure 4.2(a) point out the only mismatch between the two distributions. These are two erroneous pixels, but although running many more iterations on the sample, the algorithm was not able to correct this error, which obviously corresponds to a local minimum that is difficult to escape. The reason the current algorithm is not able to escape this minimum, is that

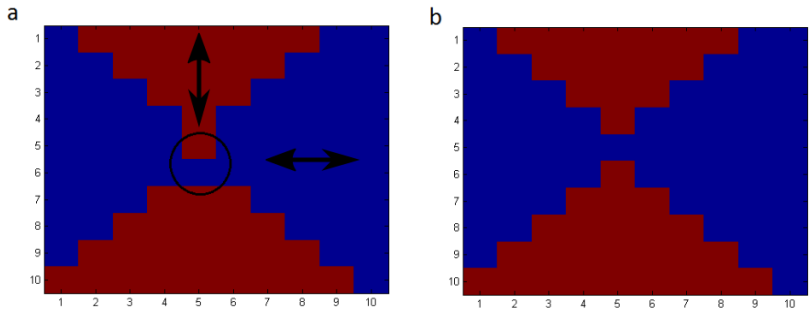

Figure 4.2: The SAXS tomography orientation retrieval algorithm applied to a synthetic 10x10 system. Blue colour pixels are areas with particles oriented at 0°, and red indicates areas with particles oriented at 90°, indicated by the arrows. a) is the result after convergence, starting out with an initial random distribution. b) is the configuration that was attempted to retrieve. The simulation was done with 10 annealing cycles with 400 attempted Monte-Carlo steps per cycle, T_0 was set to 300 and δT was 0.8, ξ was 0.

getting the correct configuration would have to happen in two steps: First the red pixel has to be changed to blue, then the blue has to be changed to red, or vice versa.

Similar results obtained when increasing the system size to 100x100 pixels, still with only 2 possible domain orientations, can be seen in Figure 4.3. There is a clear match between the retrieved distribution, and the input distribution to be retrieved. It should be noted that the interfaces between the areas in Figure 4.3(a) are not sharp as they are in (b). This makes the distribution seem random in these areas and its hard to distinguish where the interface between the large areas of the different orientations is located. Some of these errors may be due to the same effects described regarding the 10x10 system, but is also likely due to the retrieval algorithm not running long enough. It can be seen from Figure 4.4 that the energy is still decreasing after 80000 iterations, but at a very slow rate. Meaning that most attempted Monte-Carlo steps are rejected, indicating that the algorithm would have had to run for quite a lot longer to be able to correct these seemingly random areas. The correct solution has similar energy as many other configurations since the change in energy from changing one voxel is relatively small compared to the total energy of the system.

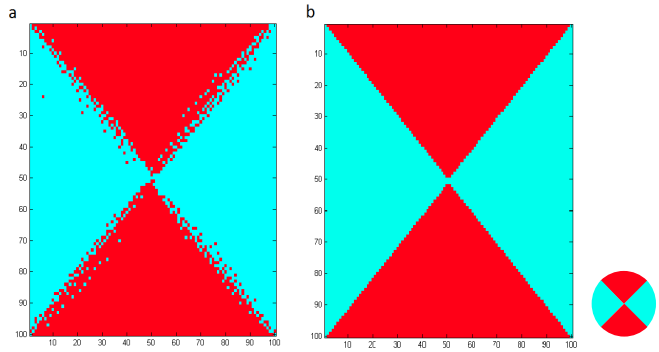

Figure 4.3: The full method applied to a 100x100 system, with 2 possible orientations. The orientations corresponds to angles in the colour wheel in the bottom right corner. Figure a) is the resulting distribution after the simulation originating from a random initial distribution. Figure b) is the distribution attempted to retrieve. The simulation was done with 20 annealing cycles, with 4000 Monte-Carlo steps during each cycle. T_0 was set to 400 and δT was 0.95, cost was 0.

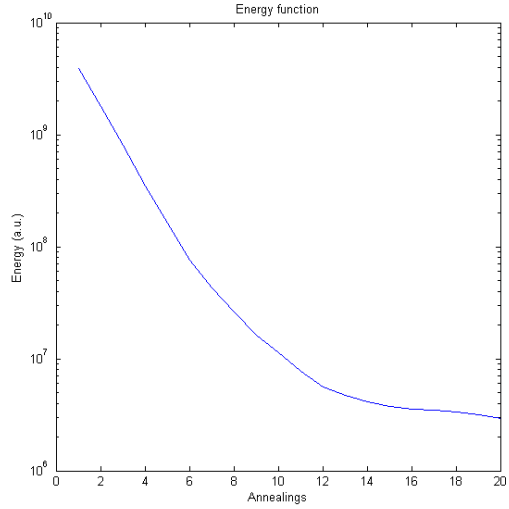

Figure 4.4: Plot of the energy of the 100x100 as a function of annealing cycles. The energy has been multiplied with a factor 10^{-6} to reduce round-off errors caused by the double precision numbers at large values. Note the logarithmic scale. The plot shows how the energy function behaves by decreasing rapidly in the start, then slower and slower as the system converges.

The previous distributions that were attempted to retrieve were both heavily biased by how the experimental data will look, and they were both squares. To show that there is nothing special with these shapes, and that more than 2 possible orientations can retrieved, various shapes were tried. The results from these retrieved orientations can be seen in Figure 4.5 and Figure 4.6. The algorithm was able to retrieve the orientation distributions with little or no error.

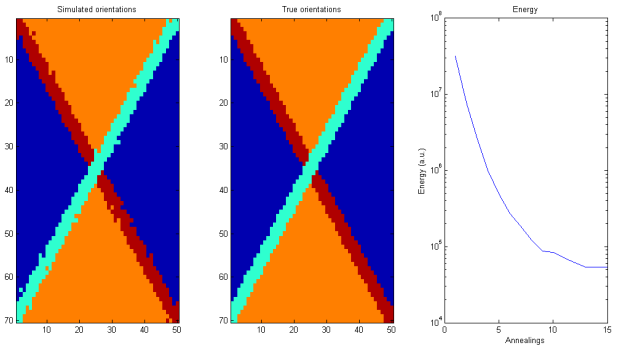

Figure 4.5: The single voxel method applied to a 50x70 system with 4 possible orientations. a) the retrieved distribution. b) the distribution to be retrieved, and c) is the energy plot. 15 annealing cycles with 8000 Monte-Carlo steps per cycle, T_0 = 600 and δT = 0.8 and $\xi = 0$ was used.

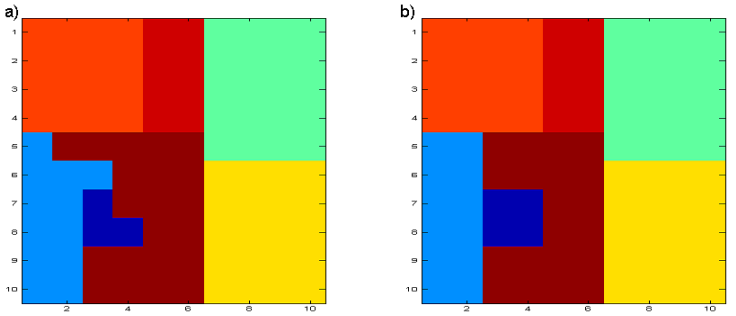

Figure 4.6: The single voxel method used on a 10x10 system with 7 possible orientations. a) the retirieved distribution, and b) the distribution to be retrieved.

4.2 Retrieving Orientation Distribution from Experimental Data

4.2.1 The Unconstrained Energy Function

Figure 4.7 shows the retrieved orientation distribution for experimental SAXS data, assuming four different orientations. Corrections for absorption is calculated on the experimental data. The red and light blue areas show that the talc particles orient themselves with the surface normal parallel with the surface normal of the iPP sample, which corresponds well with what we already know about the sample. However the in between orientations (purple and green) only show tendencies towards certain areas and are not clustered together to form a larger area of the same orientation. Still these tendencies show good resemblance with the earlier results in Figure 3.2, where these in between orientations go along the diagonals of the sample This retrieval went on for 463 000 Monte-Carlo steps and as can be

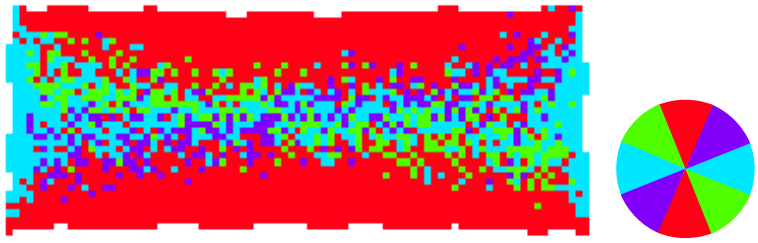

Figure 4.7: Retrieved orientation distribution assuming 4 possible orientations. The colouring of the different regions corresponds to angles as indicated by the colour wheel. 463 annealing cycles each where 1000 attempted Monte-Carlo steps were performed with $T_0 = 5{\cdot}10^{-5}$ and $\delta T = 0.99$, ξ was set to 0.

seen from Figure 4.8, the system enters a local minimum after 30 annealing steps. For the rest of the retrieval algorithm it attempts to escape these local minima, but ends up in other local minima. Note that the energy increases, which emphasises a main advantage of simulated annealing: it can temporarily go to a higher energy in attempts to escape the local minimum it is in.

Figure 4.9 shows the result after running the retrieval algorithm for 35 an-

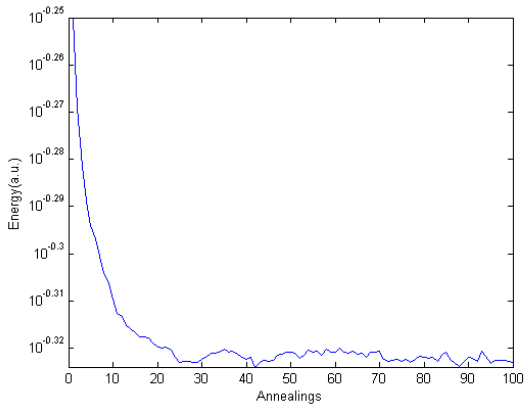

Figure 4.8: Energy plot of simulation to retrieve figure 4.7. This plot only goes to 100 annealing steps whereas the full simulation went to 463. Between 100 and 463 the energy only oscillates around the same value and gives no more interesting features.

nealing cycles each with 1000 Monte-Carlo. This distribution was retrieved by correcting for absorption on the simulated scattering data instead of on the raw data. The same tendencies can be seen in this case for the regions with talc particles oriented at $\pm$ 45° where they align along the diagonals of the sample. However, these regions are still spread over a large area. Some

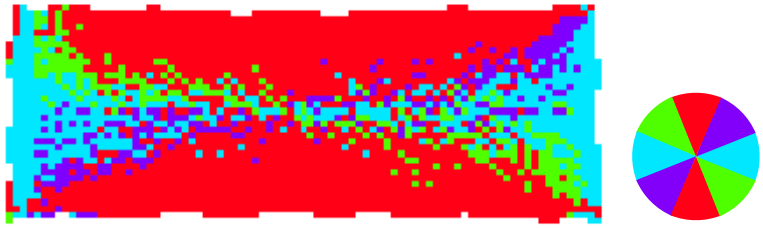

Figure 4.9: Retrieving the orientation distribution with 4 possible orientations. The simulation was done with 35 annealing cycles with 1000 attempted Monte-Carlo steps per cycle. The temperature T set to $8{\cdot}10^{-5}$, and δT set to 0.98 . Additional cost was set to zero.

artifacts that should be noted are in the corners, where there are small regions that do not match the surrounding orientations nor do they match the true distributions. Those are most likely a case where the shape of the

simulated sinogram does not match the experimental sinogram due to the mismatch between the real iPP sample and the theoretical sample used to simulate SAXS tomography.

4.2.2 Gradients of Slowly Varying Spatial Parameters

It has to be noted that in all attempts at retrieving the orientation distributions in this chapter, the value of the cost ξ in Equation (3.3) has been set to zero. Figure 4.10 shows the distribution where the ξ has been set to a large value. The shape it retrieves is closely related to the true distribution, but it also introduces new artifacts that can be seen especially in the middle of the figure, where the imposed favorization of continuous regions becomes dominating in the results.

Figure 4.10: Retrieving the orientation distribution from experimental data assuming 2 possible orientations. The value of the cost term was set high to emphasise how it controls the simulation. The retrieval was done over 56 annealing cycles with 1000 Monte-Carlo steps per cycle.

4.2.3 Multiplying the Scattering Intensities With a Q^n Factor

Retrieved orientation distribution when the cost function is multiplied by a factor Q^3 to emphasize higher Q data, can be seen in Figure 4.11. This is much the same case as with no Porod factor, but here the green and purple areas are spread on a much smaller area of the sample and not reaching far into the neighbouring regions. The same artifacts in the corners can also be observed here.

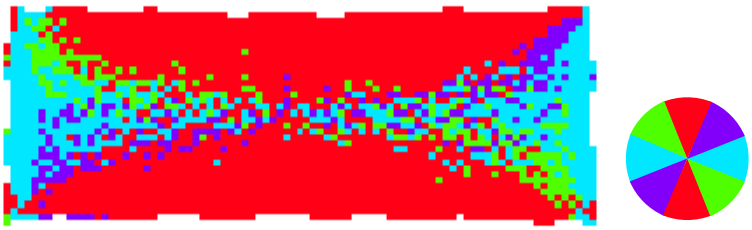

Figure 4.11: Retrieving the orientation distribution from experimental data assuming 4 possible orientations. The simulation was done with 35 annealing cycles each with 1000 attempted Monte-Carlo steps. The SAXS sinograms were multiplied by a factor Q^3. The temperature T set to $8 \cdot 10^{-5}$, and δT set to 0.98 . Additional cost ξ was set to zero.

In Figure 4.12 the energy function was multiplied by a factor Q^4. An alteration of the algorithm was done by instead of changing one and one voxel at a time, regions containing several voxels were changed at a time. The size of these regions was reduced as the energy converged. No annealing schedule was used when the algorithm changed groups of voxels at a time and only favourable energy steps were allowed. When the algorithm reached the point of changing single voxels each Monte-Carlo step it started using an annealing schedule, and returned to allowing unfavourable energy steps. The experimental data used here were of a different cross section of the sample to show that different cross sections contain the same orientation distribution of the talc particles, as would be expected. In these distributions the green and purple regions have connected into larger continuous regions in-between the red and light blue regions. It has a strong resemblance to previous results from these samples in Figure 3.2.

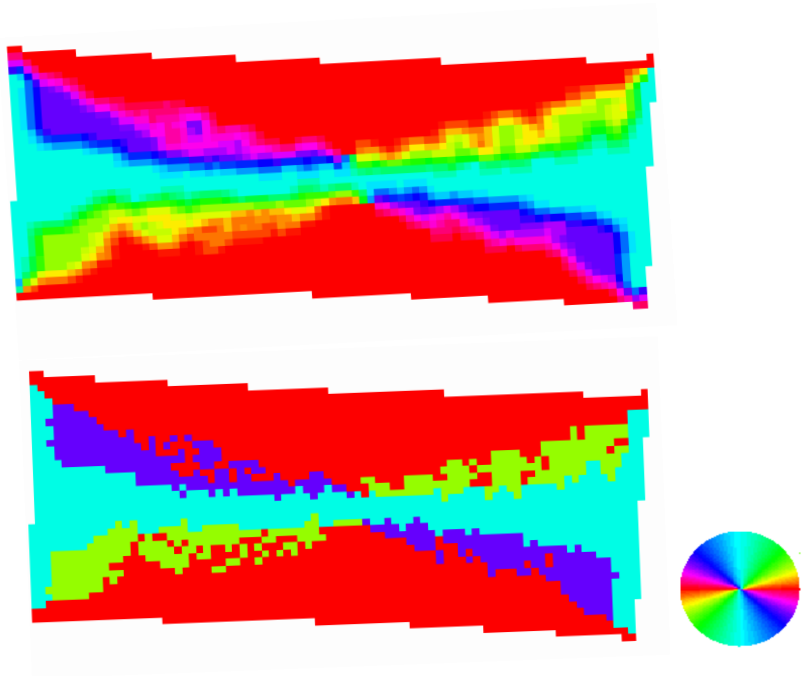

Figure 4.12: Retrieved orientation distribution on another cross section of the iPP sample. On the upper figure an averaging function has been used to create a smooth transition between the regions in the directly retrieved distribution. The orientation of the particles are indicated by the colour wheel. This distribution was retrieved doing 2000 Monte-Carlo steps when changing 3x3 voxels, then 2000 steps changing 2x2 voxels then another 10^5 changing one and one voxel. When changing 3x3 and 2x2 voxels no annealing schedule was used, and only favourable energy steps were accepted. When changing single voxels the initial temperature was set to $8{\cdot}10^{-5}$ with δT = 0.98. ξ was set to 0.

Chapter 5

SAXS Tomography Discussion

5.1 Optimising The Code

The difference in the CPU runtimes between the single value matrices and the full matrices in Figure 4.1 showed great promise in reducing the required time to retrieve the orientation distributions. This originates from the way that MatLab does the Radon transform where it does not calculate a value in the matrix if it is already zero. It may be possible to reduce the CPU time required by the transform even further, but that would require tailoring make a Radon transform implementation to the specific purpose. When retrieving the orientation distribution from experimental data on this theoretical sample that contain 2851 regions, the required time for the algorithm to attempt 20 000 Monte-Carlo steps went down from 8 hours to 2 hours.

5.2 Retrieving Orientation Distributions from Simulated Datasets

Figure 4.2 shows a perfect agreement between the retrieved distribution and the true distribution except for those to interchanged voxels, where the energy function has entered a local minima. The purpose of simulated annealing is for the system to be able to increase the energy in order to escape local minima. In this particular case two very specific events would have to occur in succession, and the temperature would have to be high enough

to allow them to happen. Since it is a random search algorithm, it will attempt to change all possible orientations on the sample, so if it were able to correct the interchanged voxels in the middle, it should be able to create the same undesired effects around the whole interface between the red and blue areas. The reason for these minima are linked to how the Radon transform is done in Matlab and that in this case only scattering from theoretical samples were compared. What can be seen in Figure 3.8 is that Matlab splits each region into four smaller regions. Due to the different positions of these smaller regions they will be interpolated into different bins, and two neighbouring large regions will be interpolated into some of the same bins. Those bins that they share will have close to the same value if the two neighbouring regions of different orientations swapped orientations. When comparing with experimental data this splitting of the voxels may be beneficial for retrieving the orientation distribution, since it is a way of giving a width to the projection beam which makes it closer related to how the X-ray beam in the experiments has a finite width. The beam width of the computed projections is something that has not been discussed in this thesis.

In Figure 4.3 there is a diffuse region near the reconstructed interface between the large red and light blue regions, which should have been a sharp interface. This is an issue of system size. The energy plot on Figure 4.4 shows that the energy is still decreasing, however quite slowly. As the system converges toward an energy minimum, most of the voxels will have the correct orientation. The algorithm searches randomly and will attempt to change the orientation in already correct voxels meaning that the time between each successful Monte-Carlo step increases as the energy decreases. For this system size it took 80000 attempted Monte-Carlo steps to reach that configuration. To reach the perfect distribution it would probably require several times more, and even then it might not be able to perfectly retrieve the distribution due to the local minima of interchanged voxels as discussed above. Then it becomes an issue of how much details are required. In this case both the red and light blue regions of the true distribution are quite large and there are only those two possible orientations. The algorithm is able to retrieve the large overall features and the effects along the interface are acceptable. However, if finer details in more complex systems than this one are required, then these effects may become detrimental.

It was clear that from comparing the horizontal scattering from theoretical datasets that minimising the energy in Equation (3.2) is a way of retrieving the orientation distribution. In addition working with synthetic known datasets made it possible to gain a deeper understanding of the effects of the algorithm that could be of use when retrieving the distributions from experimental data.

5.3 Retrieving Orientation Distribution from Experiments

5.3.1 The Unconstrained Energy Function

Figures 4.7 and 4.9 shows the retrieved orientation distributions with an unmodified cost function. They both show good resemblance with the true distribution, with the red and light blue areas along the edges indicating that the talc particles align themselves with their surface normal parallel with the outer edge normal of the iPP sample. They also have the tendencies of the green and purple areas, representing the in between orientations, going along the diagonals of the sample cross section. However, these in between orientations do not gather together in continuous regions and create uncertainties of their exact location.

In the real iPP sample the orientations of the talc particles can take any possible direction. Still when attempting to retrieve the spatial distribution of orientations with our algorithm, a certain (low) number of discrete orientations have to be chosen. This will result in areas where the real particles have orientations not matching any of the directions chosen for the retrieval algorithm, having to take either of the discrete orientations. When also taking into account the swapped voxels discussed in the previous section, it will be hard for the algorithm to find the optimal solution due to all the local minima. A graphical explanation of this with two possible orientations can be seen in Figure 5.1. This will result in many areas where the discrete orientations do not match the true orientation to seem quite random.

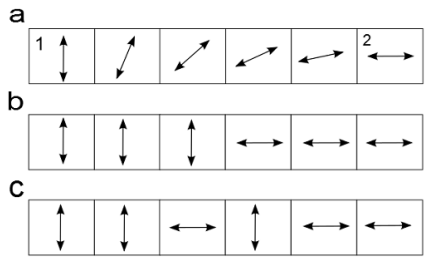

Figure 5.1: How the optimal solution may differ from a local minima solution. 1) and 2) indicate the two discrete orientations used to retrieve the orientation distribution. a) The true orientation distribution, b) the optimal solution the algorithm can accomplish if two discrete orientations are assumed, c) the case of a local minimum.

Our attempts at retrieving the orientation distributions were done with either two or four allowed discrete orientations in the reconstruction. This is due to the purple and green regions being spread over a relatively large area of the sample, making it hard to determine exactly where they are supposed to be. Increasing the number of possible orientations in the reconstruction, the distribution seemed completely random and yielded no further information regarding the orientation distribution.

The artifacts in the corners and along the edges of the retrieved orientation distributions in Figures 4.9 and 4.11 are most likely occurring due to mismatches between the theoretical sample and the real sample, and the simulated sinogram not perfectly overlapping with the experimental one. The shape of the theoretical sample is just an approximation, and when MatLab performs its rotation methods during the radon transform there will be a lot of edgy features that are not present in the real sample. The sinograms were aligned to each other by manually inspecting the number of projections that hit the sample and where the centre of the sample should be. This involved trial and error and the best matches were picked, but small misalignments are found to not impact the results significantly.

5.3.2 The Gradient Term

The additional cost term on the energy function was aimed at reducing the effects described above and making the voxels of different orientations stick together to make up larger regions of the same orientation. All retrieved distributions described in the previous chapter, except Figure 4.10, were done with the value of the cost ξ set to zero. This is due to the difficulty of finding a suitable value for this constant. When retrieving the orientation distribution it would either be too small and not have any significant impact on the result, or it would be too high and too heavily influence the results. The shape of the retrieved distribution in Figure 4.10 clearly resembles the true distribution, however there are also indicators of how the cost term take control. These effects became too challenging to control when the number of possible orientations exceeded two. When retrieving orientation distribution in Figure 4.10, the cost term was set very high just to demonstrate the effects it created even with only two possible orientations.

To be able to use the cost term it must be analysed more rigorously. To put it proportional to the difference in energy when changing from one orientation to another might seem like the most logical option, but if the number of allowed discrete orientations in the simulation increases, the number of possible cost values increases and finer more slowly varying features must be found.

5.3.3 Multiplying With a Q^n Factor

Figure 4.11 shows the retrieved orientation distribution where a factor of Q^3 has been multiplied into the cost function. In these images the range of how far the $\pm 45^\circ$ orientations protrude into the red and light blue regions is arguably a bit shorter, restricting these regions to a smaller area. Another feature that came with introducing the Q^n factor was that the retrieval algorithm converged faster towards the minimum. Figure 2.2 shows how the scattered intensity varies as a function of Q. With no Q^n factor the intensity decreases rapidly as Q increases, which makes the energy depend almost solely on the contributions for the low Q values. In this Q-range the difference in the form-factor $F(Q)$ for different orientations are small, making the scattering at various angles challenging to distinguish by differences in the energy function. When the Porod factor is added, the energy will de-

pend more on the higher Q-values thus making them easier to distinguish and create larger relative differences in the cost function.

In Figure 4.12 the cost function has been multiplied by a factor Q^4. In that distribution the purple and green regions are restricted to large continuous regions. When the result was smoothened through an averaging filter, the distribution shows great resemblance to previously obtained results with other methods, see Figure 3.2.

If the additional cost ξ is set to zero there is no part of the cost function that favours continuous regions of equal orientation. Minimising the cost function is then only concerned with creating the "correct" scattering intensities by going the correct distances through regions of the various orientations. No restriction was put on their position in the sample. By changing larger regions of voxels at a time at the start of the procedure, the retrieved distribution was forced to consist of continuous regions of the same orientation. In addition, by changing several voxels larger improvements can be done in the energy space than by changing a single voxels at a time. This makes it possible to dodge many local minima as the energy increases, and can also be regarded as a way of escaping local minima.

5.4 Problem Size and Further Work

The results of Figure 4.12 by changing regions of voxels at a time shows great promise for further work and increasing system complexity. The first obvious continuation would be to increase the number of possible orientations in the reconstruction to see if the method is able to retrieve greater details of the orientation distribution of the talc particles. The next obvious step could be to increase the number of voxels in the theoretical sample used in the retrieval algorithm. This will make it possible to obtain higher resolution in the retrieved distribution.

However, increasing the size and number of possible orientations will make the method require a lot more computation time to converge. With the current theoretical sample and only four possible orientations the algorithm requires more than 30000 attempted Monte-Carlo steps to reach a stable solution, and with the single voxel method it used about 1 hour per 10000

Monte-Carlo steps. The theoretical sample used here was using 1/16 of the voxels of a theoretical sample that was constructed to look like a cross section of the real iPP sample. The single voxel method presented in this thesis ensures that the required time to do the computations do not depend as heavily on the number of regions in the theoretical sample, but a relatively large increase in required time for the retrieval algorithm to converge since the orientation of more regions have to be retrieved.

Time requirement may be of no significance to the results the method is able to obtain, it may however be of great interest to the one carrying out the analysis. There are a lot of variables and scaling factors included when retrieving the orientation distribution. Such as scaling to match the distance the projections go through the sample, scaling to match the scattering intensities, temperature of the system and absorption coefficient. These create a lot of uncertainties and making adjustments to them may affect the results, i.e. retrieving the orientation distribution must be done several times for different sets of variables.

The experimental data used in the thesis was only a subset of the complete experimental dataset. The SAXS tomography experiments were done with a step size of 0.5° between each linescan. Only the data from every 1° increase were used. It would then also be of interest to use the additional experimental data and analyse if more detail of the orientation distribution can be obtained through these data, and how much detail can be obtained with a given size of the experimental dataset.

The talc particles were previously found to have a preferred orientation along the injection axis. When simulating scattering data and retrieving the orientation distribution, this originally three-dimensional problem was reduced to two-dimensional problem by assuming all talc particles to have their surface normal perpendicular to the injection axis. The form-factor of the talc particles could then be calculated only in the Q_θ direction. Figure 3.4 shows the positions on the detector used to make the experimental data used for the reconstruction. From the shape of these sectors it is evident that even when assuming one direction of the talc particles to be fixed the experimental data will still contain a lot of scattering from the Q_z direction. Even if only experimental data in the Q_θ direction were to be used, this data would also contain scattering from other directions of the talc particles.

This is because of deviations in the z direction of the talc particle surface normals that occur in real samples. The final goal of SAXS tomography is to be able to retrieve the full three-dimensional orientation distribution of particles of similar properties as talc. Retrieving the distribution of the deviation from perpendicularity to the injection axis of the talc particles surface normal using the same regions of the detector as this thesis, could be an intermediate step towards using complete scattering data.

Applying constraints of slowly varying spatial gradients modelled in the way done in this thesis showed no hope of improving on the retrieved results in the desired way. It is however a concept that should be able improve and stabilise the results, and other methods of applying this should be investigated.

Further analysis of the properties of the method will be of great value when expanding the use of it to analyse other, similar samples. And towards using the method to retrieve the full 3-dimensional orientation distribution of particles using the whole scattering signal.

Part II

Variable Illumination Computational Microscopy

Chapter 6

Optical Microscopy Theory

In another part of the electromagnetic spectrum is the region of visible light, which compared to X-rays have very low energy. The difference in energies causes visible light to have quite different interactions with matter, which in large part can be modeled by refractive indices. The refractive index does not only depend on the material in which the electromagnetic wave is propagating but also on its wavelength, called *dispersion*. For X-rays the real part of the refractive index, which determines how much the wave will be refracted at an interface is close to unity, so refraction can be disregarded in most cases. However, for visible light this is often not the case causing refraction at these frequencies to depend on the energy of the wave and its angle of incidence.

In optics there are two ways of describing the optical system, either with wavefronts or as rays. Wavefronts consider how the optical components modify the wavefront by changing its direction or curvature. Rays are straight lines perpendicular to the wavefront along which the energy flows. Tracing these rays using geometrical properties of the system is essential for the detailed design of optical instruments [15].

6.1 Geometrical Optics

Electromagnetic waves propagating through a homogeneous medium with refractive index n will travel at a phase velocity $v = c/n$. It can be shown

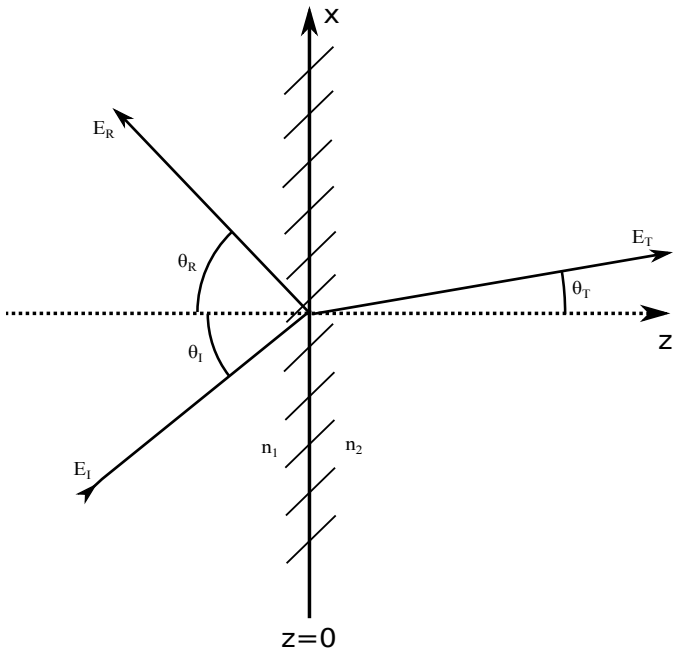

Figure 6.1: A flat boundary located at $z = 0$ between two media with refractive index n_1 and n_2 where an electromagnetic wave E_I is incident resulting in a reflected E_R and transmitted E_T wave. The waves make angles θ_I, θ_R and θ_T respectively with the surface normal.

from Maxwell's equations that at a boundary between two homogeneous media with dielectric constants ϵ_1 and ϵ_2 containing no free charges or currents the following boundary conditions must hold

$$\begin{aligned} &(i)\epsilon_1 E_1^{\perp} - \epsilon_2 E_2^{\perp} = 0 \quad (ii)B_1^{\perp} - B_2^{\perp} = 0 \\ &(iii)E_1^{\parallel} - E_2^{\parallel} = 0 \quad (iv)\frac{1}{\mu_1}B_1^{\perp} - \frac{1}{\mu_2}B_2^{\perp} = 0 \end{aligned} \tag{6.1}$$

Let a plane wave $\boldsymbol{E}_I(\boldsymbol{r}, t)$ be incident on such a boundary located at $z = 0$ with incident angle θ_I to normal vector of the boundary. It will then be scattered at the interface into a reflected wave $\boldsymbol{E}_R(\boldsymbol{r}, t)$ and transmitted wave $\boldsymbol{E}_T(\boldsymbol{r}, t)$.

$$\boldsymbol{E}_I(\boldsymbol{r},t) = \boldsymbol{E}_{0,I} e^{i(\boldsymbol{k}_I \cdot \boldsymbol{r} - \omega t)} \tag{6.2}$$

$$\boldsymbol{E}_R(\boldsymbol{r},t) = \boldsymbol{E}_{0,R} e^{i(\boldsymbol{k}_R \cdot \boldsymbol{r} - \omega t)} \tag{6.3}$$

$$\boldsymbol{E}_T(\boldsymbol{r},t) = \boldsymbol{E}_{0,T} e^{i(\boldsymbol{k}_T \cdot \boldsymbol{r} - \omega t)} \tag{6.4}$$

$\boldsymbol{E}_0$ gives the amplitude and polarisation of the respective waves. A sketch is given in Figure 6.1 The boundary conditions from Equation (6.1) must hold for all points on the interface at $z = 0$, thus all the exponential factors must be equal. All three waves have the same angular frequency ω giving that

$$xk_{I_x} + yk_{I_y} = xk_{R_x} + yk_{R_y} = xk_{T_x} + yk_{T_y} \tag{6.5}$$

must hold. From this the three fundamental laws of geometrical optics can be derived. First, the law about the plane of incidence, which says that the incident, reflected and transmitted wave vectors form a plane. Second, the reflection law

$$\theta_I = \theta_R. \tag{6.6}$$

And third, the law of refraction, or Snell's law

$$n_1 \sin(\theta_I) = n_2 \sin(\theta_T) \tag{6.7}$$

which is essential to understanding optical components. If the angle of incidence is small, i.e. almost normal to the interface, the approximation $\sin(\theta) \simeq \theta$ is valid and Snell's law becomes

$$n_1\theta_1 \simeq n_2\theta_2. \tag{6.8}$$

this is called the paraxial approximation. Geometrical optics using this approximation is called Gaussian optics.

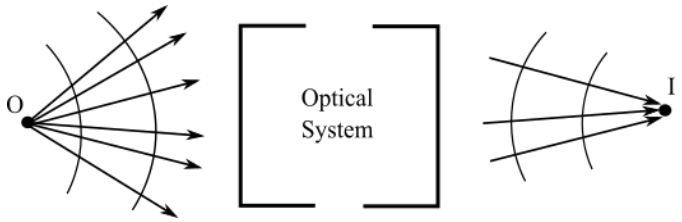

Figure 6.2: Graphic representation of a general imaging system. Rays normal to spherical wavefronts leave a point object O. Part of the wavefront gets intercepted by the optical system which in turn reflects and refracts the rays to converge on the image point I

It should be noted that there are two other ways of deriving the laws of geometrical optics when applied to the interface between two media, Huygen's principle and Fermat's principle. Huygen's principle states that every point on the leading wavefront may be regarded as a secondary source of spherical waves that themselves travel at the speed of light in the medium. At a later time the envelope of these wavefronts will constitute the wavefront. Fermat's principle says that when light travels between two points, it will choose the path where the optical path length is at a local extremum, most often a mimimum.

6.1.1 The Thin Lens

In optics it often gets referred to object space and image space. Object space is where the optical system gets its inputs from an object, and image space is where it gives its outputs. To first define the concept of perfect imaging. A point O in object space will emit spherical wavefronts with rays going out radially. Some of these rays may enter the optical system which can be any configuration of reflecting and refracting surfaces. If the system makes these rays converge to a single point I in real image space, this point is called an image point. Figure 6.2 shows a graphical representation of this situation of stigmatic imaging. By Fermat's principle every ray starting at O and ending up at I must have the same transit time. By the law of reversibility, if all rays change directions all rays starting at I will end up at O. In an ideal imaging system only the rays originating at O that are intercepted by the optical system will pass through I [16].

Before continuing a sign convention has to be specified for which sign to put on distances and angles, it is however important to be consistent with the chosen convention when doing calculations. We chose the 'real-positive', which stands for 'real positive, virtual negative'. Rays converging on a real image or object point will be taken as positive, and virtual images where the rays are converging in a virtual image or object point are taken as negative. Virtual image points are when the rays at some point seem to converge, or diverge, on a point that do not form an actual image in the system [15]. In Figure 6.2 the distance from the object point to the optical system will be positive, since the rays diverge from a real object point, and the distance from the system to the image point will be positive since the rays converge to a real image.

Applying Snell's law and the sign convention on a point object on axis in a medium with refractive index n_1, where the rays will be refracted at a spherical surface with radius of curvature r_1 into a medium with refractive index n_2 will lead to the general equation

$$\frac{n_1}{s_1} + \frac{n_2}{s_1'} = \frac{(n_2 - n_1)}{r_1}. \tag{6.9}$$

Here s_1 is the distance from the surface to the point object, and s_1' is the distance from the surface to the image. It works for both convex and concave surfaces. If now there is another spherical surface in the opposite of the first one such that the two surfaces make up a thin lens, the second surface has distances s_2 and s_2' and radius of curvature r_2. The thickness t of the lens is small compared to other distances in the system and the relation $s_2 = t - s_1'$ can be approximated to $s_2 = -s_1'$. It may seem counter intuitive that s_2 becomes negative, but as can be seen on Figure 6.3 it describes the distance from the virtual image point to the second refracting surface, thus the sign agrees with the sign convention. Putting together Equation (6.9) of the first and second surface results in

$$\frac{1}{s_1} + \frac{1}{s_2'} = \frac{n_2 - n_1}{n_1}\left(\frac{1}{r_1} - \frac{1}{r_2}\right). \tag{6.10}$$

The focal length of a thin lens is defined as the image distance of an object at infinity, meaning that when parallel rays hit the lens they will converge

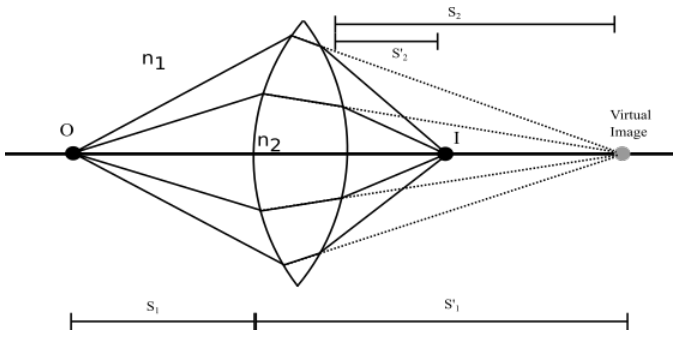

Figure 6.3:
Rays diverging from object point O and converge on image point I. The virtual image point is where the rays would have converged if they had only been refracted at the first surface of the lens.

at the focal point. This results in the lens equation of a lens of refractive index n_2 immersed in a medium of refractive index n_1

$$\frac{1}{f} = \frac{n_2 - n_1}{n_1}\left(\frac{1}{r_1} - \frac{1}{r_2}\right). \tag{6.11}$$

It should also be noted that the lens equation applies for both convex and concave lenses just that the sign of the focal length will differ since the image point will change between real and virtual.

6.1.2 Magnification and Ray Tracing

Until now the image and object point have been assumed to be on the optical axis, however Equation (6.11) also applies for objects and images off-axis. Let there be a lateral object of height h_0. Each point of the object will act as a point source of spherical wavefronts with rays going in all radial directions. A ray tracing diagram of rays coming from the top point of the object can be seen in Figure 6.4. The ray going parallel with the axis will go through the focal point at the other side of the lens. In the small angle approximation the ray going through the centre of the lens will be refracted at two almost parallel surfaces, and since the lens is thin the parallel displacement of the ray will be negligible. The last ray going through the left focal point will go through the lens and come out parallel with the optical axis. These three rays will intersect at a point h_1 below the optical axis. Ray

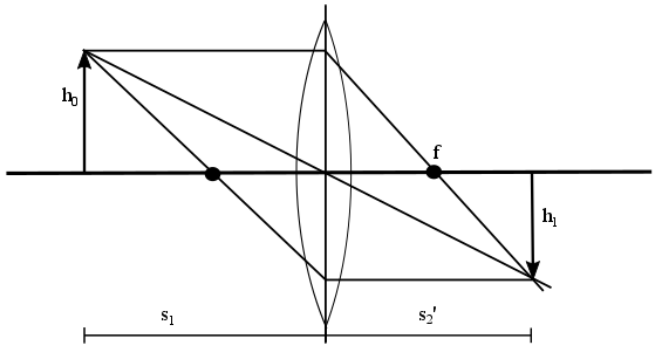

Figure 6.4: Raytracing on a convex lens. The rays parallel with the optical axis will go through the focal point on the right side, while the rays going through the focal point on the left side will exit the lens parallel with the optical axis. The ray going through the centre of the lens will be moved parallel but can be neglected since the lens is thin.

tracing of every point on the object, will construct conjugate image points between the optical axis and h_1, thus this is where the image will form. By inspection of the image it is easy to figure out the lateral magnification of the lens

$$m = -\frac{h_1}{h_0} = -\frac{s_2'}{s_1}. \tag{6.12}$$

The minus sign is added due to the sign convention. With the real-positive convention both s_2' and s_1 are positive, however the figure shows that the image is formed below the optical axis and the magnification must be negative. In the previous cases many approximations can be made since the lens is thin. If the lenses get too thick that it can no longer be neglected, more thorough computations are required. These operations have been simplified by looking at the reflections, refractions and propagation through various media as a transformation of the ray. By setting up these transformations as matrices, the transformations can be put together by simple matrix multiplication. This will not be covered here, it is however useful to know of its existence [16].

6.2 Aberrations

In the previous section on geometric optics every object point was mapped to an image point. Every ray from the object point went through its conjugate image point. In reality this is not the case. Few optical components are capable of creating perfect images, and even then they put great restriction on both the object and the image. It can be shown that to form a perfect image the magnification of the optical system has to be the ratio between the refractive index of the object plane and image plane [15]. Reflecting and refracting surfaces capable of perfect imaging are called Cartesian surfaces. The simplest example of such is a plane mirror, a plane refractive surface however only approaches perfection for rays which are nearly normal to its surface. Another example is an ellipsoid mirror, though it has only one object point and one image point, namely the two foci of the ellipse. One of the few refracting objects capable of perfect imaging is the double hyperbolic lens, though the concept of perfect imaging only applies for a single point object at a set distance on-axis from the lens. A perfect image of a surface can be achieved using a spherical lens, however the object outside the lens must be a spherical surface, and the image points will be inside the lens, also making up a spherical surface. In summary these systems are so case specific that it is a lot easier to accept that perfect imaging of a general system does not exist, and rather try to minimise the aberrations that occur.

There are three main contributions to the degradation of image quality. Light scattering, aberrations and diffraction. Light gets partially reflected at surfaces, and may be scattered by inhomogeneities in a transparent medium. These effect causes loss in image intensity, but when rays from a different object point gets scattered through the image point it will start damaging the quality of the image, this is what is called aberrations. Even with an ideal imaging system there are limitations to how good the resolution of the image can be. The limited size of the optical system only uses part of the full wavefront causing diffraction and blurring of the image. Systems limited by diffraction are said to be *diffraction limited*.

There are two ways of treating aberrations. When a wavefront converges to an image point they have to be perfectly spherical to converge at a single point. How the wavefront is distorted from the perfect sphere is called *wave aberration*. The ray aberrations can be found by simply drawing the

normal lines to the wavefront to see by how much the rays miss the ideal image point. The two approaches lead to the same analytic result, but the wave aberration tend to lead to a clearer physical picture.

The most significant aberrations are the third order Seidel aberrations that come forth when the power expansion of the sine and cosine functions are extended to include up to the third power, instead of only the first which is used in Gaussian optics. When the third power of the expansions is used, the difference between the ideal wavefront and the real wavefront for a point Q on the wavefronts when refracted on a single spherical surface can be shown to be [15]

$$\begin{aligned} a(Q) =& C_1 r^4 + C_2 h' r^3 \cos(\theta) + C_3 h'^2 r^2 \cos^2(\theta) \\ &+ C_4 h'^2 r^2 + C_5 h'^3 r \cos(\theta). \end{aligned} \tag{6.13}$$

Here r is the size of the aperture, h' is the height of the image and θ is rotation around the optical axis. The C's are the Seidel constants.

6.2.1 Spherical Aberration

The first term in Equation (6.13) is called spherical aberration. It is unique in the sense that it is the only aberration that exists when both object and image are on the optical axis and depend only on the size of the aperture. When light is refracted at higher angles of the lens, they hit farther and farther away from the ideal image point. In a system where the optical axis goes in the z-direction, the rays at the extremes will miss by a distance b_z along the axis, and a lateral distance b_y from the image point. Somewhere within the distance b_z from the ideal image point is a point giving the best image for the specific system, and the broadening of the point object compared to this image is called 'circle of least confusion'. Figure 6.5(a) shows how an on axis object point gets imaged with spherical aberrations. Rays hitting the outer edges will miss the paraxial image point more up to the maximum b_z. Object points off axis will also have image points that miss in the lateral direction. All image points will be spread within a sphere around their optimal image point, hence the name spherical aberration.

For a given aperture size the effects of spherical aberration are often minimised by the use of aspherical lens surfaces, special combinations of con-

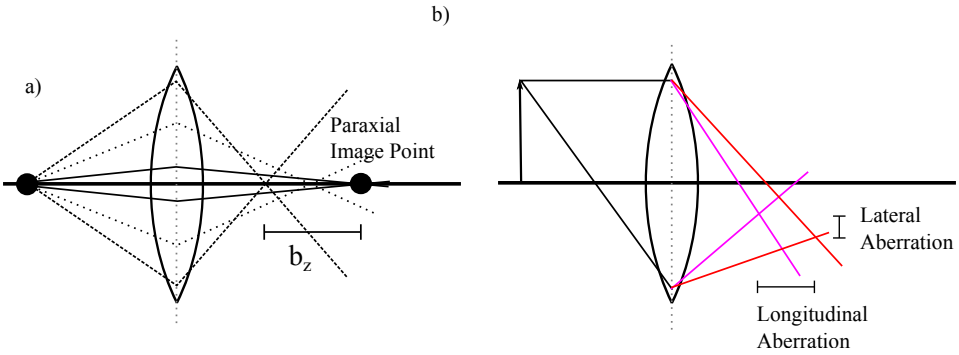

Figure 6.5: a) How the paraxial approximation becomes less valid at higher angles and cause spherical aberrations, the different line types are just to more easily keep track when tracing a ray. b) How light with different wavelengths have different image points and cause chromatic aberrations. The colour of the rays indicate the colour of the light.

vex and concave lenses, or by decreasing the size of the aperture. The corrections are generally made to minimise aberrations of points at a certain distance from the lens.

6.2.2 Chromatic Aberration

All considerations above have been done under the assumption of monochromatic waves in the system thus elegantly bypassing the phenomenon of dispersion. Generally the refractive index depends on the wavelength of light such that different wavelengths will refract at different angles on a surface and thus give the focal length a wavelength dependence. This is called chromatic aberration. An on-axis point will only have longitudinal aberrations, while an off-axis point will have both longitudinal and lateral aberrations. Figure 6.5(b) illustrates how light of different wavelengths will have different image points.

Chromatic aberrations can be corrected by either only using a monochromatic light source or by adding multiple lenses of varying refractive power to the system to effectively cancel the chromatic aberrations caused by each other.

6.3 Instrumentation In Optics

6.3.1 Aperture- and Field Stop

An aperture stop is often introduced to an optical system. When in position it will decrease the amount of light entering the system. It can work to reduce the number of rays from an object, thus reducing the effects of aberrations. It can also block noise and scattered rays from optical components. Finally, the apertures can be used to control the depth of field, see below.

6.3.2 Numerical Aperture

The numerical aperture (NA) is a measure of how much light an optical (microscope) system is able to collect. It is a measure of how large the cone of light from a axial object in focus that is accepted by the optical system. It is defined as

$$\text{NA} = n \sin(\alpha) \tag{6.14}$$

where n is the refractive index between the object and the lens, and α is the highest angle between the optical axis and rays entering the system. It should be noted that for a microscope with air between the sample and objective the maximum NA is 1.

6.3.3 Depth of Field

When capturing images with a camera, the object distances will generally vary a lot over the object space. However the distance from the lens to the sensor where the images are captured, will remain constant. Let the sensor be at a distance s' from the lens with no aberrations. Then an axial point a distance s will be imaged perfectly on the sensor. However, two other points at positions $s + x_1$ and $s - x_2$ will not make perfect point-like images at the sensor, but instead appear as diffuse dots. Figure 6.6 shows how different object distances will create different object sizes on a fixed sensor caused by different image distances. The resolution of the sensor image is then limited by how large the diffuse dots are. If a given resolution is wanted, object points within distances x_1 and x_2 of the focal point O that are imaged on the sensor within the resolution are said to be in the depth

of field DoF of the imaging system. If the acceptable diameter of a point source is d, and the diameter D of the lens hit by rays from an object at s_O the depth of field DoF can be expressed as [16]

$$\text{DoF} = \frac{2Ads_O(s_O - f)f^2}{f^4 - A^2d^2s_O^2} \tag{6.15}$$

Here f is the focal length of the lens, and $\text{F}\# \equiv f/D = A$ commonly called the f-number or relative aperture. D is the diameter of the aperture of the lens. The chosen acceptable diameter d sets a threshold of a maximal resolution for images of an object within the depth of field.

Equation (6.15) is resolution specific. Various adaptations that assume near diffraction limited optics exist for different applications. One that is often used for microscopes is given by

$$\text{DoF} = \frac{\lambda}{\text{NA}^2} \tag{6.16}$$

where λ is the wavelength of the light and NA is the number aperture of the microscope[1].

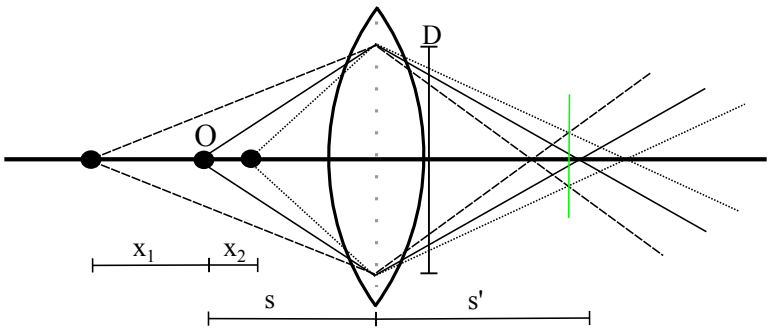

Figure 6.6: Illustration of how three on-axis objects create images at different distances in image space. If O is the object point at perfect distance to be imaged at a flat screen, the points to the sides will be imaged on the screen over a larger area. The green line shows the position where the image size of any of the points is at a minimum.

[1]Adresse to Edmund Optics: http://www.edmundoptics.com/technical-resources-center/testing-targets/gauging-depth-of-field-in-your-imaging-system/

This outline that imaging systems have a lot of different factors to take into account, with all the different types of aberrations and depth of field. This cause the design of an optical system to be tailored for specific needs by finding compromises between the different distortions of the image and the desired resolution.

6.3.4 Köhler Illuminated Microscopes

Most modern back illuminated microscopes are based on the Köhler illumination scheme and were traditionally illuminated using a halogen lamp. The rays from the lamp goes through a collector and a condenser to ensure an even diffuse illumination of the sample so that intensity differences resulting from the illumination cannot be seen on the image. This reduces image artifacts and gives a high sample contrast.

6.3.5 Confocal Microscope

If the sample in front of a microscope is thicker than the depth of field of the microscope, the resulting image will contain a lot of out of focus background. This is where the confocal microscope comes in. Instead of illuminating the sample with a uniform beam it uses a tightly focused beam. This way only a small area along the axis of illumination is imaged, called the probe volume. By putting a pinhole in front of the microscope only light from the focal plane of the microscope is allowed through filtering out the out of focus background. Since the illumination is focused onto the sample, the sample either has to be very small, or the microscope has to do a raster scanning procedure, and use the images to reconstruct the image of the sample at a given depth. If the sample is scanned at various depths a complete three dimensional image can be constructed. Giving good images, confocal microscopes require quite complex technical systems for managing the beam focus and raster scanning procedure.

6.4 Refocusing Using Varied Illumination

In the VIM the Köhler illumination scheme is replaced with a programmable LED matrix. On the panel the LED positioned at (x_i, y_i) has an illumination NA defined as [5]

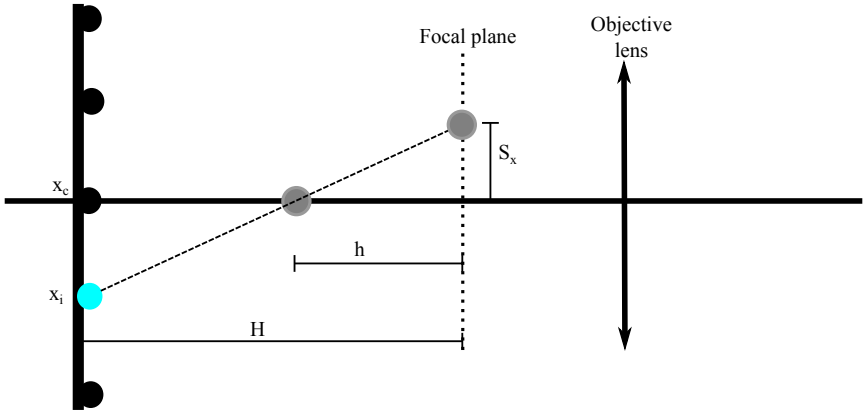

Figure 6.7: The sample at distance h from the focal plane is illuminated by LED x_i, here marked by a blue circle. The resulting image will then show an object shifted a distance s_x off the optical axis. Note that $h \ll H$ in reality.

$$\text{NA}_{illu} = \frac{r}{\sqrt{r^2 + H^2}}. \tag{6.17}$$

Here H is the distance along the optical axis between the sample and LED matrix. The radius r is given by $r = \sqrt{(x_i - x_c)^2 + (y_i - y_c)^2}$ where (x_c, y_c) is the position where the optical axis hits the LED matrix.

When a sample is positioned a distance h from the focal plane of the objective lens and illuminated by a single LED not on the optical axis and has an illumination NA_{illu} smaller than the objective NA_{obj} it will cause an image shift (s_x, s_y) of the resulting image. LEDs at different positions will cause different image shifts

$$s_{x_i}(h) = \frac{x_i h}{H} \quad s_{y_i}(h) = \frac{y_i h}{H}. \tag{6.18}$$

A conceptual sketch of how the sample a distance h from the focal plane will be projected at a height s_x when it is illuminated by the single LED at position x_i on to the focal plane, can be seen in Figure 6.7.

All these images obtained for different LED lamps will be blurred since they were taken out of focus. The method of re-focusing the images is

based on post processing the images taken with LEDs at various positions by shifting the position of the image back onto the optical axis. When images from different LEDs are merged together it will create a higher image contrast for the parts of the image that originate from the sample, while the blurring artifacts will be averaged out and become comparably small. This way the in-focus features of the sample can be recreated.

Chapter 7

VIM Procedures and Experiments

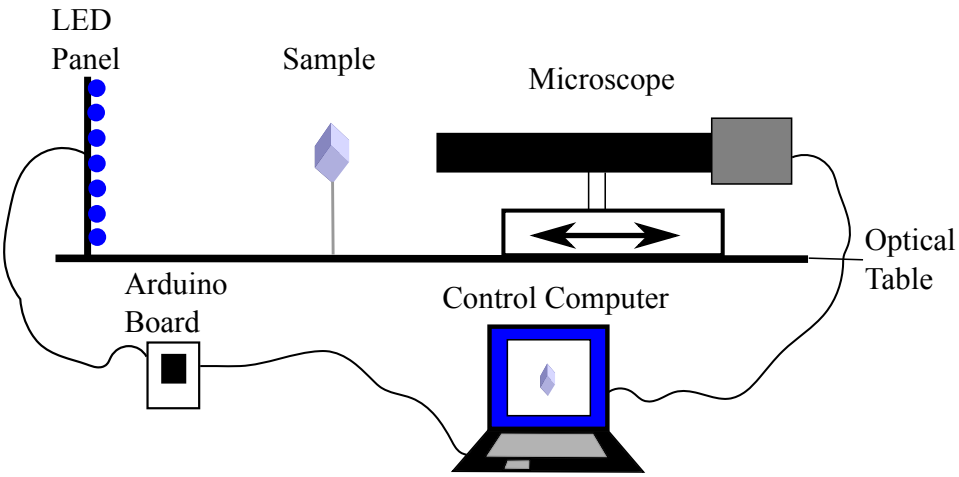

Figure 7.1: Sketch of the whole microscope setup.

7.1 Microscope Components

7.1.1 Variable LED Illumination

The illumination panel is a 32x32 LED-matrix, with one red, green and a blue LED per lamp of the matrix delivered by SparkFun Electronics[1].

[1] Homepage of SparkFun https://www.sparkfun.com/

A photography of the LED matrix can be seen in Figure 7.2. This is a cheap progressive 1/16 scanning display, which means it does not light up all LEDs at the same time, but rather display two and two rows in rapid succession. This has great advantages when it comes to wiring and power consumption, but makes it more important with a fast microcontroller and optimised code. The LEDs are controlled by twelve FD9802 LED drivers which together are able to assign a 1 bit value to 192 LEDs at a time, *on* or *off*. The panel consist of 16 regions of 16x2 lamps, which region to be lit is chosen by a demultiplexer. There are also six inputs to the panel that goes to the LED driver chips, a clock input which shifts the LED values to the register of the LED drivers and an output enable that turns on the assigned row of LED with the assigned colours in the register.

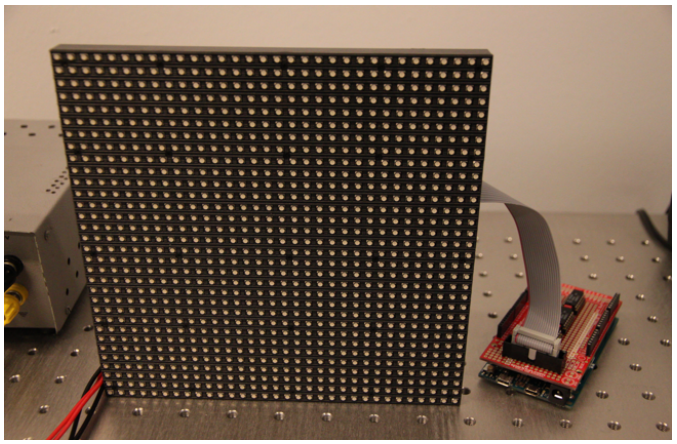

Figure 7.2: An image of the 32x32 LED matrix

The LED panel is powered by a 5V 1A DC power supply, which is not enough to power all LEDs of the panel at full intensity. If attempted it will result in an aliasing effect where regions of LEDs with high and low intensities will move across the panel. This power supply was however sufficient for the experiments done in this thesis where only a relatively small number of LEDs were lit at the same time.

The LED panel is controlled by an Arduino Due, shown in Figure 7.3. Arduino boards are open source computer hardware, based on Atmel mi-

crocontrollers [17]. They provide digital and analog I/O pins that can be interfaced with a wide variety of circuits and components, and simple methods for loading code onto the board. The Due board features an Atmel SAM3X8E ARM Cortex-M3 microprocessor. It has a 32-bit core and 84 MHz CPU clock speed. It is the first Arduino board with these high performance features making it the primary choice when calculation and speed is required, such as when operating a large LED display. The LED display can work decently with other boards, but it will require a highly optimised code and good technical insight of the microprocessor. The Due board is still quite new, meaning that the users are still in the process of discovering its possibilities and limitations. The inputs of the LED board require 5 V [18], but the I/O pins of the Due board only deliver 3.3 V [17]. The Due board and LED panel are connected through a 74HCHC04N power inverter to get the desired voltage. Connected to the hardware UART of the processor is a ATmega16U2 microprocessor providing serial-to-USB communication with the computer.

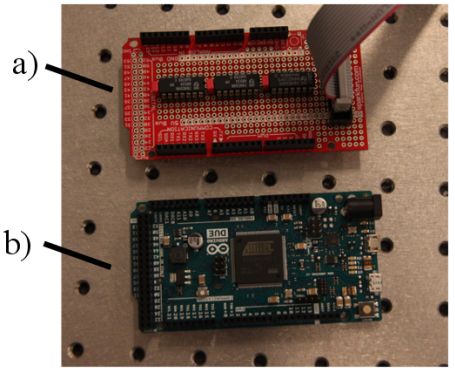

Figure 7.3: Photography of the Arduino Due board, with the shield taken off. a) the red shield for wiring the power inverters and is put on top of the Arduino to connect to the I/O pins of the Arduino. b) the Arduino Due board.

7.1.2 The Microscope

The detector unit of the microscope is a Ueye iDS 3480CP camera. It consists of a MT9P031STM CMOS sensor from Aptina. The sensor is of a 1/2" class with 2560x1920 pixels of size 2.20 μm^2. Each pixel has up to 12 bit RGB colour depth. The sensor is extraordinarily sensitive and provides

means of capturing sharp low-noise images. The camera has a wide variety of functions and is well suited for microscopy and medical technology [19].

The optics of the microscope was built from standard optical components bought from Edmund Optics[1]. Connected to the camera is a 152.5 mm optical extension tube. This tube provides a static distance between the lenses and the camera, while also preventing stray light from entering the system. The lens system consist of a 2X M plan infinity-corrected objective lens connected to a 1X accessory tube lens. The tube lens works as a connection to the extension tube while adjusting the focal length to match the length of the extension tube. The 2X lens has a numerical aperture NA of 0.055 and gives a field of view of 3.2x2.4 mm^2 on an 1/2" sensor. It has a theoretical resolving power of 5 μm. The objective lens focal length (working distance) is designed to be as much as 34.0 mm, which is practical for our purposes. It should be noted that there are no means of mechanically altering properties of the optics such as zooming or stopping apertures. However, with the use of an infinity corrected objective the distance between the objective lens and tube lens does not need to be fixed and allows for other optical components to be placed in between to modify the wavefront if necessary.

The camera is mounted on top of a Newport UTS50PP stepper motor. While the LED panel remain at a fixed position, the stepper motor provide means of changing the distance between the objective and LED panel, and thereby the position of the focal plane. It has a position accuracy of 0.3 μm [20]. The stepper motor is controlled by an Newport SMC-100PP single axis driver which is connected to the computer via USB. Figure 7.4 shows the fully mounted camera unit.

[1] Edmund Optics: http://www.edmundoptics.com/

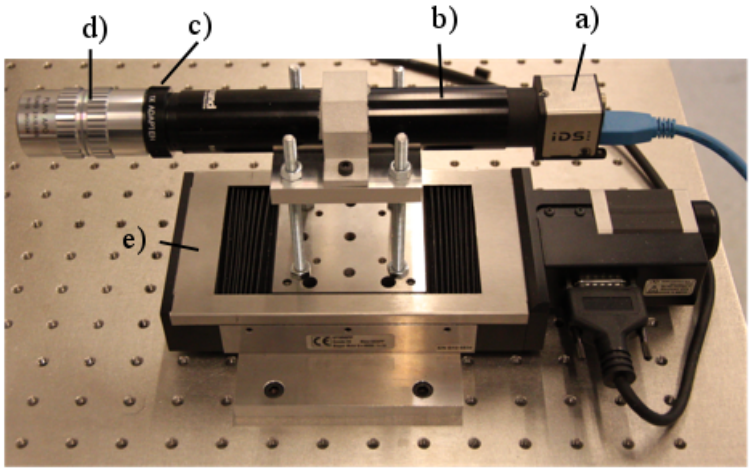

Figure 7.4: The fully mounted camera unit. a) the iDS camera. b) optical extension tube. c) 1x tube lens. d) 2x infinity corrected objective lens. e) stepper motor.

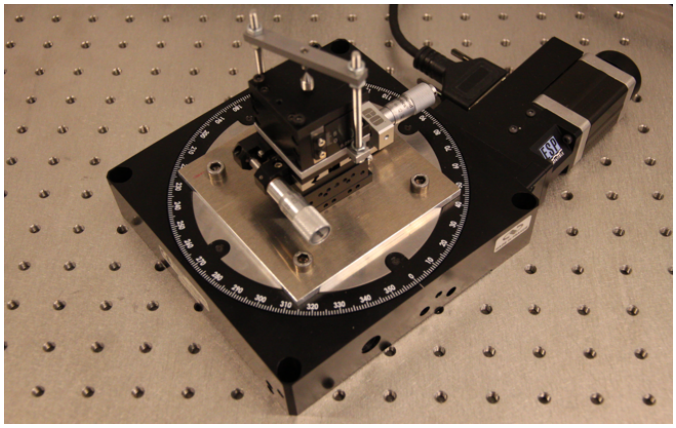

Figure 7.5: Photography of the rotation stand sample mount that is incorporated in the microscope

There is no fixed sample mount and there is physical space for whatever is needed for the experiment at hand. If needed the program for the microscope also has incorporated the possibility of a rotation stand for the sample that can be seen on Figure 7.5. The rotation stand is a Newport URS-150BPP rotation stepper motor which has a guaranteed absolute accuracy of 0.05° [20]. It is controlled by another Newport UTS50PP driver,

which is serially connected to the camera mount driver and utilise the same USB connection to the control computer.

7.1.3 Software

Software to control all components of the microscope was made. This made it possible to tailor the programs for specific needs. This section will only contain a brief introduction to the software and its capabilities. A more detailed walkthrough can be found in Appendix A.

The code running on the Arduino was written using the Arduino programming language. It can receive commands of which LEDs to display, and continues to display the LED array until the power is shut. When the Arduino is only displaying the LEDs and not taking any inputs, the LED array is updating at about 100 Hz

To control the whole imaging procedure a program with a graphical user interface (GUI) was written in Labview, which communicates with the hardware, and saves images to the control computer. The program was written with high versatility of both illumination scheme and data capturing in mind. Illumination can be chosen by which LEDs to display, and how many to display at a time. Imaging parameters on the camera can be altered. Several data sets with different sample and microscope positions using the same illumination scheme, can be captured within a single run of the microscope. To ensure that the Labview-Arduino communication went smoothly, a programmed delay of 100 ms was implemented in the Labview program after sending each command to the Arduino. The operating speed of the rest of the program is only limited by of the application program interface (API) Labview has to the other components.

7.2 Imaging Using the Varied Illumination Microscope

In measurements done with the VIM camera a square region of the LED matrix was scanned through, illuminating one and one LED per image captured. The size of the square was chosen larger with increasing distance

between the sample and LED matrix because the number of LEDs within the field of view of the microscope increased. Only blue LEDs were used. The exposure time was ∼500-600 ms on all images taken with one single LED lit, which gave high enough image contrast. No sub-sampling modes were utilised because no high-speed imaging was done.

For an experimental setup the sample was positioned at a distance H from the LED matrix, and the focal plane of the objective was set to be a distance h from the sample. In the post processing procedure the illumination NA of the LED used for a given images was calculated using Equation (6.17). For an image taken at a distance $h \neq 0$ out of focus illuminated by the LED at index position (x_i, y_i) the image shifts at the sensor were calculated by

$$s_{x_i} = \frac{Lh(x_i - x_c)}{H} M \quad s_{y_i} = \frac{Lh(y_i - y_c)}{H} M \tag{7.1}$$

where L is the distance between each LED on the panel, (x_c, y_c) is the position of the optical axis on the LED matrix, and M is the magnification of the objective lens. Refocusing to different depths of the sample was done by back-shifting the images distances

$$S_{x_i} = s_{x_i} \frac{P_x}{w_x} \quad S_{y_i} = s_{y_i} \frac{P_y}{w_y} \tag{7.2}$$

in x- and y- directions respectively. Here P_x and P_y are the number of pixels on the sensor in the x- and y- direction respectively, and w_x and w_y are the physical size of the sensor pixels. Back-shifting the images means aligning the captured images so that the part of the sample which is on axis is at the same index on all images. The easiest way to do this is by moving the sample in each image back onto the optical axis the same amount it has been shifted out by being illuminated out of focus by illumination coming in at an angle.

Bright-field imaging was done by setting $h = 0$ when capturing the images and adding together images which LED had a $\text{NA}_{illu} < \text{NA}_{microscope}$. This method should give the same result as microscopy images captured using conventional Köhler illumination[5]. *Dark-field* images were created by summing up images where $\text{NA}_{illu} > \text{NA}_{microscope}$.

Chapter 8

Results Obtained Using the Microscope

8.1 Measuring Depth of Field

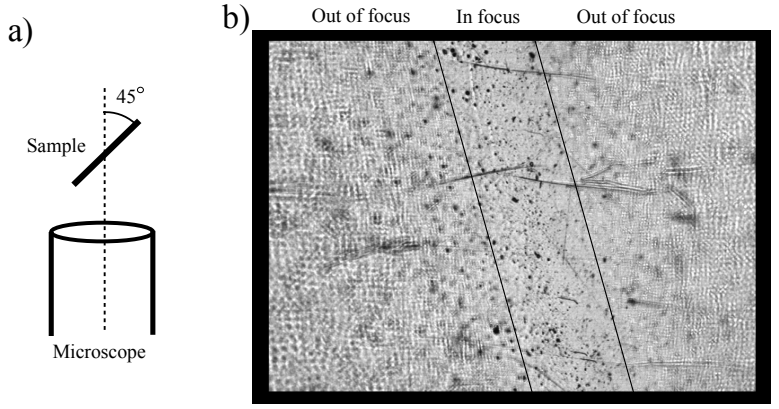

Figure 8.1: Gauging the depth of field. a) The experimental setup when gauging DoF. b) Microscope image of a thin piece of polymer used to estimate the DoF. Because the sample is at an angle with the optical axis, measuring a distance that is in focus perpendicular to the optical axis gives by trigonometry a focus distance parallel to the optical axis.

Depth of field is a quantity that depends on a lot of parameters and cannot be calculated before the imaging device is completely specified. Figure 8.1

shows a bright-field image taken of a thin piece of polymer. The polymer was positioned at an angle 45° to the optical axis. By analysing the image an estimated depth of field could be probed, yielding an estimated depth of field of ∼300 μm. This inspection is far from accurate, but can work as an indicator.

Calculating the depth of field using Equation (6.16) gave a depth of field of ∼149 μm for the objective lens with λ= 450 nm.

8.2 Bright and Dark Field VIM

Figure 8.2 shows an image taken of a semi-transparent polymer prism using 13 central LEDs lit at the same time. All 13 LEDs are well within the field of view of the microscope, effectively working as a backlight illumination. The piece of polymer was 150 μm thick, making the whole thickness of the sample within the microscope depth of field. The LED array-sample distance was 266 mm. The dots and lines are defects and damages on the surface of the polymer. The exposure time was only 200 ms to compensate for the many LEDs being lit.

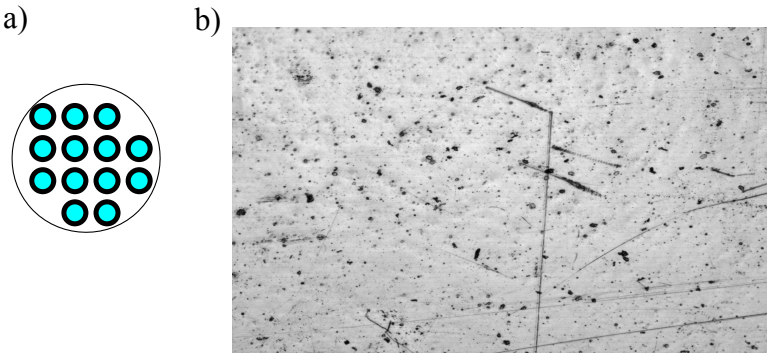

Figure 8.2: a) Positions of the LEDs used when doing bright-field imaging with the microscope. b) Microscope image of a polymer sample in focus with the 13 LEDs in figure a) lit.

Figure 8.3 shows an image of the same polymer sample but in this case the image is made up of 13 images. All images were taken with one LED lit each with $\mathrm{NA}_{illu} < \mathrm{N}A_{lens}$. By comparing Figures 8.2 and 8.3 the two

approaches clearly give the same result.

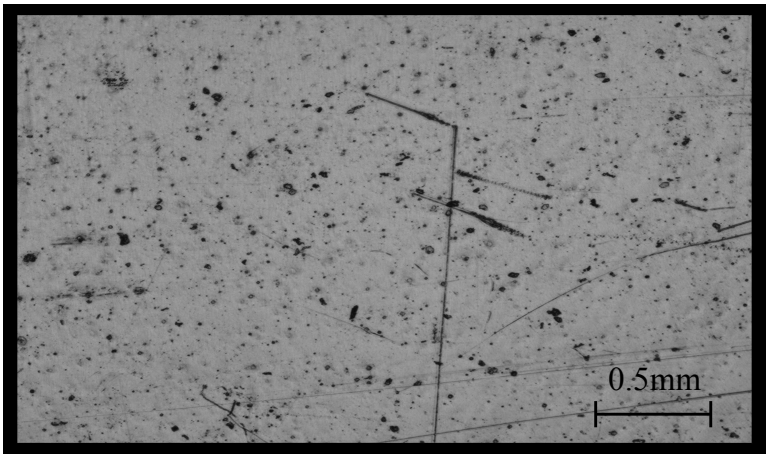

Figure 8.3: Bright-field image built up of 13 images taken with 1 LED lit each.

Figure 8.4 shows again the same polymer sample, but here the 24 images from LEDs with $NA_{illu} > NA_{lens}$ were used, giving a dark-field image. Note that the bright regions in the bright-field image of Figure 8.3 are dark in the dark-field image of Figure 8.4, and vice versa.

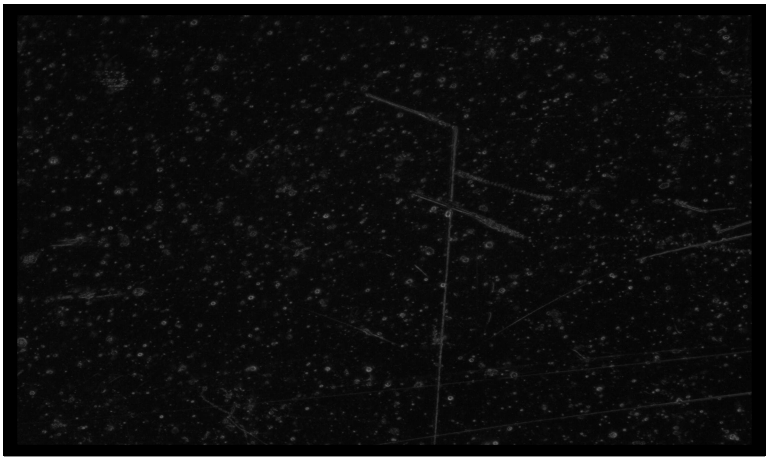

Figure 8.4: Dark-field image built up of 24 images with $NA_{illu} > NA_{lens}$ and 1 LED lit each.

8.3 Refocusing Using VIM

The refocus experiments were done by placing the sample in-focus and the sample-LED distance was kept constant for the subsequent measurements while the position of the microscope was changed using the stepper motor. Thin samples with little detail were used to emphasise the ability to refocus VIM images taken out of focus.

Figure 8.5 shows the in-focus image taken of a small copper grid used for TEM by adding up 13 images with central LEDs lit, which was used as benchmark for the refocusing images. The grid had a diameter of 3 mm. The sample-LED distance was 266 mm.

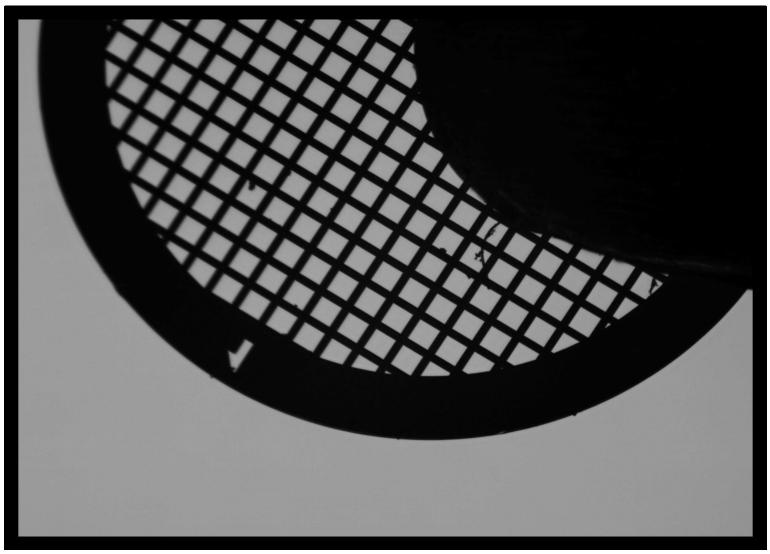

Figure 8.5: In focus image of a net made up by 13 VIM images taken in-focus.

Figure 8.6(a) shows images that were taken with the focal point moved 0.5 mm *further away* from the LED panel and naively added up. In Figure 8.6(b) each image has been shifted onto the optical axis in accordance with Equation (7.2) with h = +0.5 mm. The naively added up image is blurred as would be expected of an image out of focus. In the refocused images the lines are sharper and more detail can be seen and it resembles the in focus image to a greater degree.

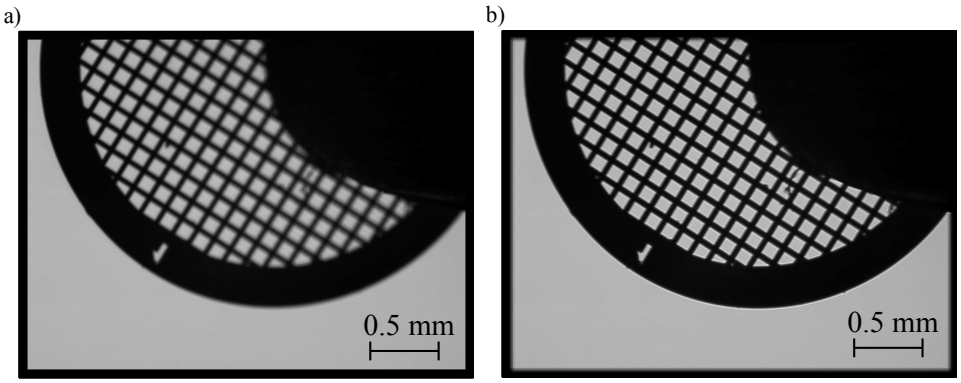

Figure 8.6: a) The sum of images for 13 different LEDs taken with the focal plane moved 5 mm *further away* from the LED panel added up with no shifting of the images. In b) each image has been back shifted onto the optical axis in accordance with LED positions and h = 0.5.

In Figure 8.7(a) images were taken with the focal point moved 0.5 mm *closer* to the LED panel and naively added up. Figure 8.7(b) shows the same images shifted onto the optical axis with h = -0.5 mm. Again the refocused image looks a lot more like the in-focus images.

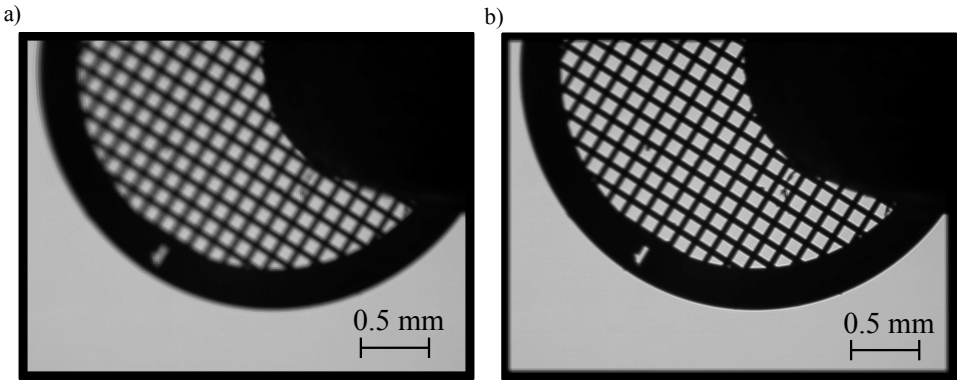

Figure 8.7: a) The sum of images for 13 different LEDs taken with the focal plane moved 5 mm *closer* to the LED panel added up with no shifting of the images. In b) each image has been back shifted onto the optical axis in accordance with LED positions and h = -0.5.

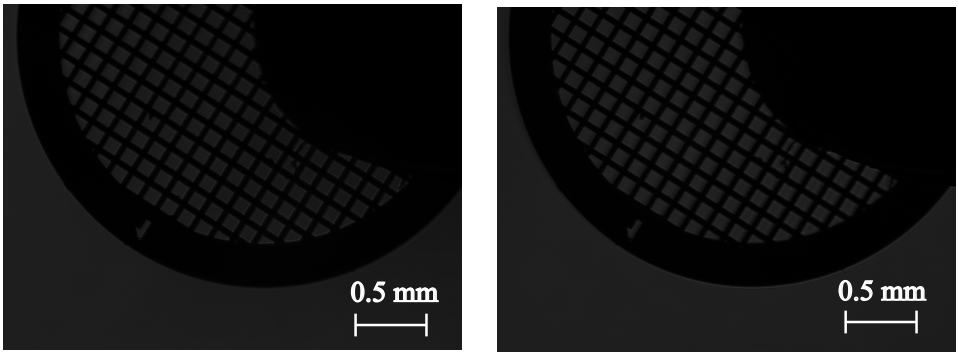

Figure 8.8: Out of focus images taken with 1 LED lit each and the focal plane moved 5 mm further away from the LED panel. These are two of the 13 images that were used for refocusing Figure 8.7.

Figure 8.8 shows two images taken with 1 LED lit each. Compared to the refocused images in Figures 8.7(b) and 8.6(b) it clearly seen that the numerical refocusing is capable of sharpening the resulting image, even though all the sub-images are obtained out of focus.

Chapter 9

VIM Discussion

9.1 The Microscope

9.1.1 Illumination

The Arduino boards are built to be compatible with a large range of different applications. This makes them great for people that are not accustomed to microcontrollers, but it puts constraints on how well it can perform a specific task. With the current code the scanning display LED panel operates at a 100 Hz frame rate. Compared to normal PC screens that operate at 60-120 Hz this is quite good. There is however no control of how long each region of the LED panel is lit at a time, which may be quite unfortunate further use of the microscope in scientific imaging. High frame rates means each LED gets little display time every scan, they do however get displayed more often. It is not known how high the average displayed intensity of the LEDs are compared to the maximum intensities either. The current code make use of high level functions built in to the Arduino. Higher frame rates are possible to achieve, it would however require a deeper knowledge of the architecture of the board in order to directly communicate with the pins of the microprocessor instead of communicating with them through the high level functions.

The LED panel is commercially available and was probably built with the intention of showing low resolution images and animations. One drawback is that there is no data sheet for it to detail its performance. All available

information of it is based on personal experience and unverified sources that have reverse engineered it. In specific regarding the LEDs themselves there is hardly any information to gather. There is no knowledge of their intensities, wavefronts or spectrum. There are methods for experimentally gauging these properties. This should be done if further analysis of the illumination scheme are to be carried out.

9.1.2 Labview Program

For this specific task Labview is practical for making good user interface and a large variety of means to communicate with different types of hardware and link them together in a single program. However, the complexity of this high level programming language often results in a slow API when communicating with different applications.One part of the microscope program where this can be problematic is in the imaging module.

With 500 ms exposure the Labview program uses on average 1.6 s per image. The pixel rate setting on the camera was 10 megapixels per second, which means it takes 500 ms to read from the sensor of the camera to the RAM of the PC. Sending the string command to the Arduino is not expected to take much time since it only involves to send information through the USB and no two-way communication. When also subtracting the 100 ms programmed delay, this leaves 500 ms just to communicate with the camera and saving the image. For the use in this thesis this does not matter, but it puts constraints to using the microscope in future high speed imaging.

9.2 Imaging Capabilities

9.2.1 Bright and Dark Field Imaging

By comparing Figure 8.2 and Figure 8.3 it is evident that using many LEDs within the field of view of the microscope to take one image is the same as adding up many images with varied illumination. There is a clear difference in image brightness, which is due to the differences in exposure times. To get good image contrast with only 1 LED lit the microscope requires to have longer exposure of the sensors. When illuminating the sample with all the LEDs lit at the same time the same exposure time would result in many

pixels on the sensor saturating, giving loss of information in the image.

The dark-field image in Figure 8.4 clearly shows a dark-field image. The parts of the sample that scatter the light away from hitting the objective lens and they create dark regions in the bright-field image, are here instead scattering light into the objective lens to create brighter regions, while the regions that do not scatter are not visible in the image.

9.2.2 Refocusing Using VIM

Comparing Figure 8.6 and Figure 8.7 with Figure 8.5 it is clear that the refocusing the image by shifting the images using Equation (refeq:pictureshift) creates a sharper image that more closely resembles the in-focus image. Finer details that are barely visible in the naively added image are easily distinguishable in the refocused image.

Images taken out of focus are expected to contain different forms of aberrations. These images are raw images from the camera with no corrections done to them before being used for refocusing. The grid used in the experiments do not contain a lot of small details that are destroyed by out of focus aberrations. If the sample contain a lot of small details refocusing the images with this method might not be able to reconstruct these features. By identifying the aberrations of the optical system it is possible to computationally correct them which will make it possible for the refocusing to retrieve even further details of the sample.

Depth of Field And Sample Thickness

Depth of field depend on the complete optical system, for this microscope it was estimated to be 200-300 μm. The most interesting use of the refocusing method is to be able to refocus to different depths of the sample without physically moving the sample or the microscope. This would require the width of the sample along the optical axis to be larger than the depth of field. Equation (6.18) is based on assumptions of small angles and thin samples, where parallel displacement of the rays as they pass through the sample is small compared to the shifting of the image. With such a wide depth of field samples that are considerably wider than this will start to

diminish the performance of the refocusing algorithm which assumes thin samples.

The Numerical Aperture of The Microscope

The NA of the objective lens is 0.055. This numerical aperture is based on the circular shape of the lens and optical system. The sensor of the camera however is rectangular, meaning that light that comes through the edges of the objective lens may not hit the detector. Another issue is with vignetting, light coming from the LEDs along the edges of the field of view of the objective lens that does not illuminate the whole sample, giving images that a partly dark-field and partly bright-field. An example of this can be seen in Figure 9.1 where the left side of the image is a bright-field image while the right side is dark-field. When refocusing this may degrade the quality of the refocused image and make it unable to reconstruct some features of the sample. These images were filtered out in the refocusing, but by doing so information regarding the sample may be lost from the bright-field part

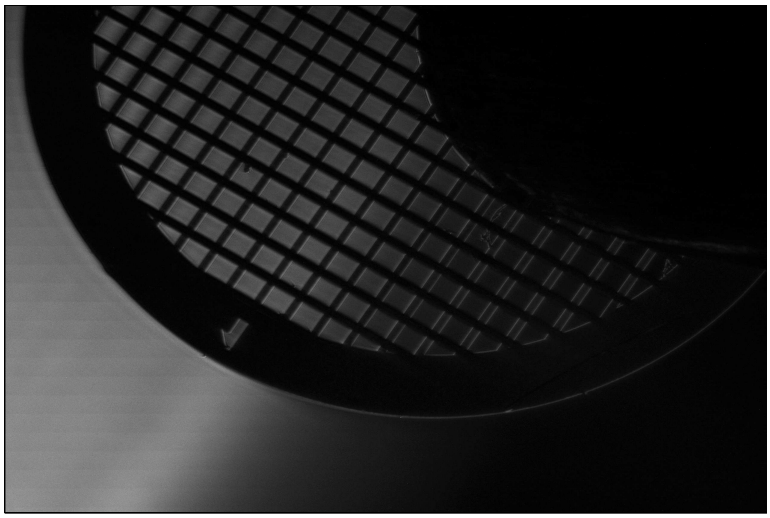

Figure 9.1: Image from an LED at the edge of the objective lens field of view. The left side of the image shows bright-field whereas the right side is dark-field

of the images that were filtered out. The dataset used for bright- and dark-field imaging consisted of 49 images. To make the bright-field image 13

microscopy images were used, and the dark-field image used 24, meaning that 12 images were filtered out indicating a possibly large loss of data.

9.2.3 Further Work With VIM

To build the microscope and demonstrate that it is capable of bright- and dark-field imaging, and that the features of the varied-illumination can be used to computationally refocus to various depths are the first important steps of its usage. There are already planned future projects with our computational microscope. The first one is Fourier Ptychography, replicating work done by Zheng [6]. The second is imaging of polymer microbeads under mechanical compression, which is of interest in our ongoing research [21]. By using the rotation stand implemented for the microscope, the goal is to do tomography scans of the microbeads and create 3-dimensional reconstructions of their surface under compression. The software developed for the microscope was constructed with both of these uses in mind. Next would be to investigate other uses made of the VIM by other research groups and determine if these methods can be of interest to the X-ray group at NTNU.

Refocusing using VIM showed good results, the method can however be further investigated. Equation (6.18) is based on the paraxial approximation. When LEDs at larger angles are lit, these approximations will become less valid. A deeper understanding of this equation to higher order approximations would help to further increase the quality of the refocusing method. It may also make it possible to refocus dark-field images. With the current optical setup the microscope has a relatively large depth of field. Altering Equation (6.18) to also include displacement of the light through a thick sample would make the microscope with the current optics more capable to investigate different depths of a sample that is several depths of field thick. The last method that will be proposed here to further improve the refocusing procedure, is by correcting for aberrations. The first of which would be to deconvolute the out of focus images with the *Airy-disc*. The Airy pattern is the result of diffraction of light when passing through a circular aperture and causes the image of a point object to be blurred [15].

Chapter 10

Conclusion

10.1 SAXS Tomography

It has been investigated if the orientation distribution of talc particles in a sample of injection molded isotactic polypropylene where the talc particles had a preferred orientation along the injection axis could be retrieved using the horizontal scattering patterns from SAXS tomography experiments. To retrieve the orientation distribution the numerical method of simulated annealing was used. Various modifications of the energy function have been presented and how they impact the obtained results.

The unconstrained cost function was able to retrieve the large features of the orientation distribution. As the number of orientations increase it was only able to retrieve tendencies of the orientations belonging to smaller regions of the sample.

Constraints of slowly varying spatial gradients were imposed on the cost function but showed little promise of improving the result. The modified cost function was able to retrieve the large features of the orientation distribution, but also introduced a lot of artifacts that made it challenging to determine if the features of the retrieved distributions were improvements or not. If this method of spatial gradients is to be used in further work, a better model should be constructed to ensure that it guides the reconstruction towards the correct solution.

Multiplying the scattered intensities with a Q^n factor yielded the most promising result for further work, especially when combined with changing the orientation of larger regions of the theoretical sample at a time. The obtained results are limited to only 4 allowed discrete orientations of the talc particles in the retrieved distribution, and show a perfect resemblance to previous results. Further investigations by increasing the number of possible orientations and increasing the resolution of the theoretical sample are advised before using the method on other samples.

In summary, it has been shown that the spatially resolved orientations of talc particles with a preferred direction inside a sample of isotactic polypropylene be retrieved by using the horizontal small-angle X-ray scattering patterns. In this specific case it was done by comparing the horizontal scattering patterns obtained through an X-ray tomography scan of the sample with simulated data of the same procedure on a theoretical sample, by minimising the presented energy function through simulated annealing. The high quality of the results bode well for further developments of SAXS tomography. This is the first time simulated annealing has been shown successful in retrieving an orientation distribution from SAXS tomography, and these results are to be published [1].

10.2 Varied Illumination Microscope

In the second project of this thesis a varied-illumination microscope has been built. The illumination scheme was a programmable LED array controlled by an Arduino board making it possible to capture images with illumination coming in from different angles. Software for capturing images, controlling the LED matrix and communicating with various motors for focusing and sample manipulation was developed using Labview.

The microscope has been presented to be able to serve as conventional backlight illumination (a la Köhler) and it has been demonstrated that capturing a single in focus image with several LEDs lit is equivalent to adding together several images with a single LED lit each. The microscope has also been demonstrated to be able to do dark-field imaging.

Utilising the properties of images taken with varied illumination it has been

shown that images deliberately taken out of focus can be digitally refocused. Several ways of improving the refocusing done with images taken with the microscope were discussed.

The control programs created for the microscope were developed with further work with the VIM in mind. They offer a high versatility in operation modes of the microscope and are ready to use for already planned projects.

Bibliography

[1] E. T. B. Skjønsfjell, T. Kringeland, H. Granlund, K. Høydalsvik, A. Diaz, and D. W. Breiby. Retrieving the orientation distribution function of embedded microscopic particles by saxs tomography. Work in progress. 2015.

[2] E. T. B. Skjønsfjell. Mapping orientation distribution of talc particles in polypropylene by small-angle x-ray scattering tomography. Master's thesis. Norwegian University of Science and Technology, 2013.

[3] J. M. Feldkamp, M. Kuhlmann, S. V. Roth, A. Timmann, R. Gehrke, I. Shakhverdova, P. Paufler, S. K. Filatov, R. S. Bubnova, and C. G. Schroer. Recent developments in tomographic small-angle x-ray scattering. *Physica status solidi (a)*, 206(8):1723–1726, 2009.

[4] T. H. Jensen, M. Bech, O. Bunk, M. Thomsen, A. Menzel, A. Bouchet, G. Le Duc, R. Feidenhans'l, and F. Pfeiffer. Brain tumor imaging using small-angle x-ray scattering tomography. *Physics in medicine and biology*, 56(6):1717–1726, 2011.

[5] G. Zheng, C. Kolner, and C. Yang. Microscopy refocusing and dark-field imaging by using a simple led array. *Optics letters*, 36(20):3987–3989, 2011.

[6] G. Zheng, R. Horstmeyer, and C. Yang. Wide-field high-resolution fourier ptychographic microscopy. *Nature photonics*, 7(9):739–745, 2013.

[7] H. Granlund, J. B Floystad, M. Esmaeili, E. T. Bakken, M. Bech, P.E Vellum, and D. W. Breiby. Mapping structural gradients in isotactic polypropylene using scanning wide-angle x-ray scattering. *Polymer*, 54(7):1867–1875, 2013.

[8] J. M. Rodenburg, A. C. Hurst, A. G. Cullis, B. R. Dobson, F. Pfeiffer, O. Bunk, C. David, K. Jefimovs, and I. Johnson. Hard x-ray lensless imaging of extended objects. *Physical review letters*, 98(3):034801 1–4, 2007.

[9] A. M. Maiden, M. J. Humphry, F. Zhang, and J. M. Rodenburg. Superresolution imaging via ptychography. *Jorunal of the optical society of america*, 28(4):604–612, 2011.

[10] M. Esmaeli, J. B. Fløystad, A. Diaz, K. Høydalsvik, M. Guizar-Sicairos, J. W. Andreasen, and D. W. Breiby. Ptychographic x-ray tomography of silk fibres hydration. *Macromolecules*, 46(2):434–439, 2013.

[11] K. Høydalsvik, J. B. Fløystad, T. Zhao, M. Esmaeli, A. Diaz, J. W. Andreasen, R. H. Mathiesen, M. Rønning, and D. W. Breiby. In situ x-ray ptychographic imaging of high-temperature co2 acceptor particle agglomerates. *Applied physics letters*, 104(24):241909 1–4, 2014.

[12] J. Als-Nielsen and D. McMorrow. *Elements of modern x-ray physics*. Wiley, 2nd. edition edition, 2011.

[13] D. J. Griffiths. *Introduction to electrodynamics*. Pearson, 3rd. edition edition, 2008.

[14] D. W. Breiby and E. J. Samuelsen. Quantification of preferential orientation in conjugated polymers using x-ray diffraction. *Journal of polymer science part b; polymer physics*, 41:2375–2393, 2003.

[15] F. Graham Smith, T. A. King, and D. Wilkins. *Optics and photonics, an introduction*. Wiley, second edition edition, 2008.

[16] F. L. Pedrotti S.J. and L. S. Pedrotti. *Introduction to optics*. Prentice-Hall, second edition edition, 1993.

[17] Arduino homepage. http://www.arduino.cc/.

[18] Led panel hookup guide on adafruit. https://learn.adafruit.com/32x16-32x32-rgb-led-matrix/overview. The guide is for the 16x32 panel of same type.

[19] Ids imaging development systems gmbh homepage. https://en.ids-imaging.com/.

[20] Newport corporation homepage. http://www.newport.com/.

[21] J. B. Fløystad, E. T. B. Skjønsfjell, M. Guizar-Sicairos, K. Høydalsvik, Jianying He, J. W. Andreasen, Z. Zhang, and D. W. Breiby. Quantitative 3d imaging of densification, delimination and fracture in a micro-composite under compresseion. *Advanced engineering materials*, 17(4):545–553, 2015.

[22] J. Mertz. *Introduction to optical microscopy*. Roberts and Company, first edition edition, 2010.

Appendix A
Programming the Microscope

Here a description of the programs created to operate the microscope will be presented. The program running on the Arduino was written in the Arduino programming language which is an adaptation of the Processing software and Wiring projects [17]. Operating the camera, communicating with the Arduino ,and controlling the motion motors were done using Labview. This section will not contain a full walkthrough of the code but contain the key elements with the general flow of the program, and the important choices that were made.

A.1 Arduino

The RGB states of the panel are stored as three 32x32 matrices that give a direct correspondence to the real world. When lighting the LEDs, the program iterates through these matrices and fills the registers of the LED drivers. When the LEDs are displayed they are either *on* or *off*, resulting in a 3-bit colour range on each pixel of the panel. When Labview sends a byte of data to the Arduino, it will be stored in the serial buffer. The Arduino will then look for a formatted string of characters, containing an entry character and a termination character. If the entry character is not present, the program will empty the buffer and go back to idle display-viewing and wait for new input. A flow chart of the Arduino operating procedure can be seen in Figure 10.1. The strings accepted by this procedure are 11-13 bytes long, and the serial buffer size is 64 bytes by default. This means that the buffer will fill up, and may cause unpredictable errors, if the send-receive-

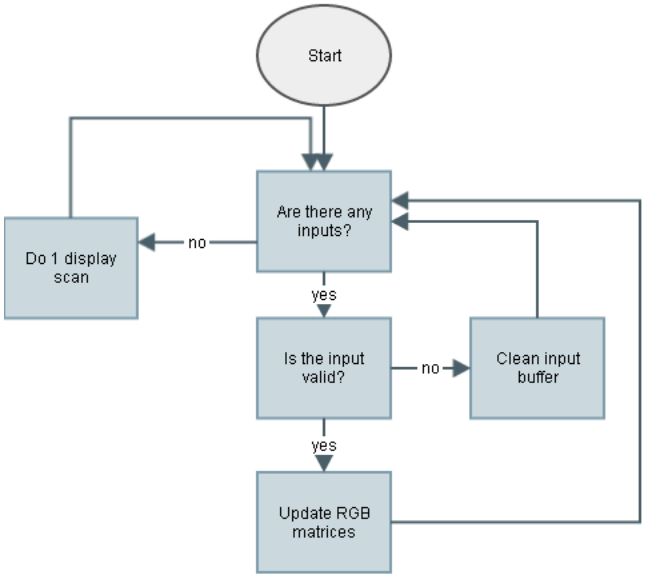

Figure 10.1: Flow chart of how the Arduino operates. It does not contain a stop node since the program will loop until the power is cut or the reset button is pushed.

read procedure is not properly managed. This is fixed by a 25 ms delay in the Arduino program, and a 100 ms delay in the Labview program. The difference in delay also take into account the different operating speeds of the Arduino and the PC and the time required to transfer the data. The data transfer rate was set to 9600 bps (bits per second), meaning that each valid message takes 10 ms to transfer, the extra delay is added to ensure no bugs occur.

When the Arduino is only displaying the array and not taking any inputs the LED array is updating at about 100 Hz.

A.2 Labview

Labview was chosen as framework for the whole microscope. This is due to its easy and user friendly possibilities to make a good looking graphical user interface (GUI). A flow chart of the general procedure of the Labview program can be seen in Figure 10.2.

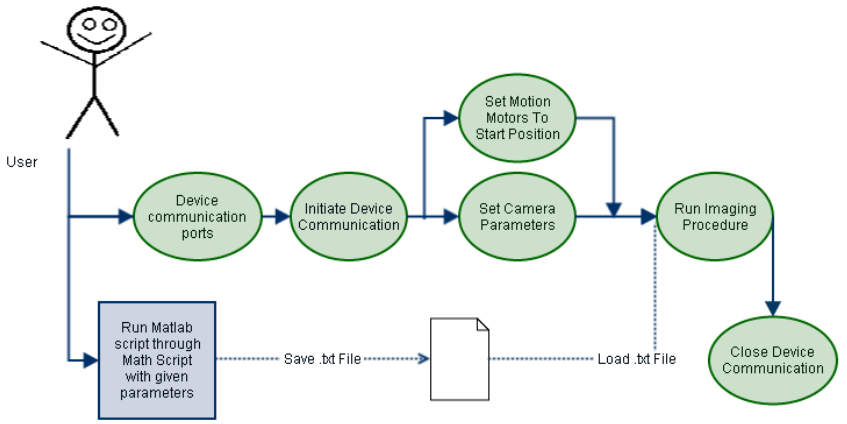

Figure 10.2: Flow chart of the general microscope program. The user has to set starting parameters and run the program.

Before starting the program the user has to interact set constants for the program. These include which region of the LEDs that will be used, and if the Matlab script should generate the LED indices in random order when generating the text file. The colour of the LEDs, when they should be lit, and how many that will be lit during each image capture, ranging from one to all chosen LEDs, has to be set. The user has to set starting position for both stepper motors, the increment wanted for each motion step and how many motion steps. There is also an option to set a subsampling mode, which will reduce the number of pixels on the camera sensor used when imaging and thus data loss and is not recommended to use. Subsampling means to not read out some of the sensors in the camera thus reducing the resolution of the resulting image and is a direct loss of data. It may only be useful if the camera is used for live video viewing at high frame rates to reduce readout time from the sensor.

The first module runs a Matlab script that generates a text file of the coordinates of the LEDs. This could have been done in Labview but not without a high increase in unnecessary complexity. The Labview-Matlab application program interface (API) is in general slow, but the scripts are small and with the use of built in vectorized Matlab functions this does not cause a significant time delay. Then the program opens up communication with the

various components. The camera uses a dotNET interface for communicating with its own API. The standardisation of dotNET makes it possible to control the camera from a wide variety of applications without having to tailor anything for each specific system. The Arduino and the motion controllers both use the virtual instrument software architecture (VISA) of Labview, which has become the standard way of serial communication with USB devices. The VISA automatically translates any character it sends into 1 byte ASCII codes that the device understands without having to manually translate the signal.

The parameters of the camera has to be set after the program has started communicating with it. This is because the pixel clock, frame rate and exposure are dynamic variables that value ranges and step sizes depend on each other. The operating procedure can be seen in Figure 10.3. *Pixel rate* sets how fast data will be read from the sensor after an image is captured (in units of megapixels per second). *Frame rate* says how fast images will be captured in frames per second, it is only useful if many images are captured consecutively but it still has to be set in any camera mode due to how exposure time depends on it. *Exposure time* says how long the sensors will actively capture data for each exposure.

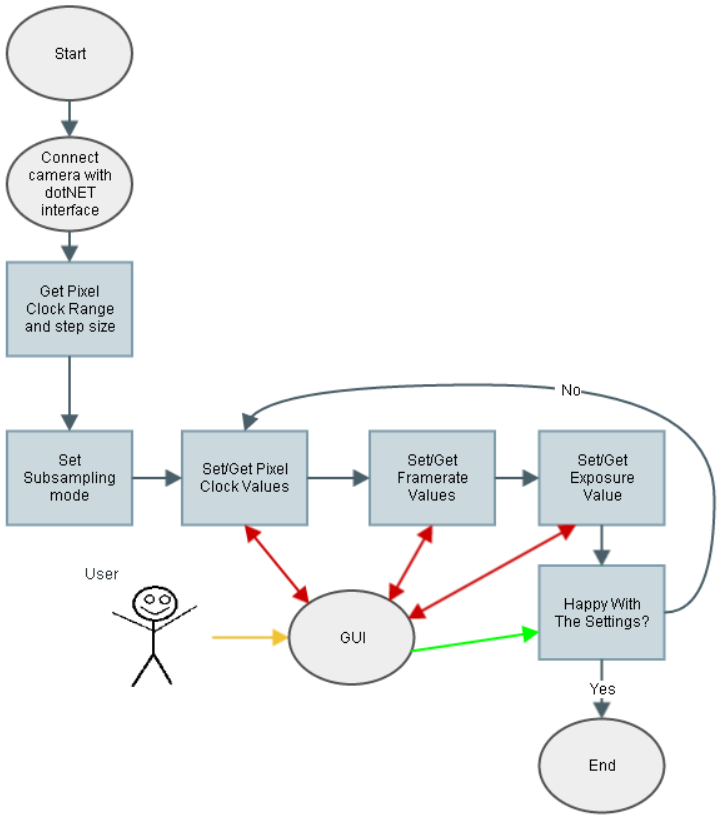

Figure 10.3: Flow chart of how the dynamic parameters are set. As each parameter is set the value ranges of the others will vary. Labview communicates the possible value ranges to the user through the GUI and the user sets new parameters through the GUI. It will run until the user closes the loop.

In the next module the text file previously generated is read and put into a string array. After sending, the programmed delay discussed above is implemented before the camera starts capturing an image. After the given exposure time is finished the camera reads the data to the RAM of the control computer and saves the image. After all images have been taken in accordance with the user defined parameter values, all communication channels are properly closed to prevent errors from occurring if the program is immediately run again. Figure 10.4 shows a flow chart of how the imaging procedure is done.

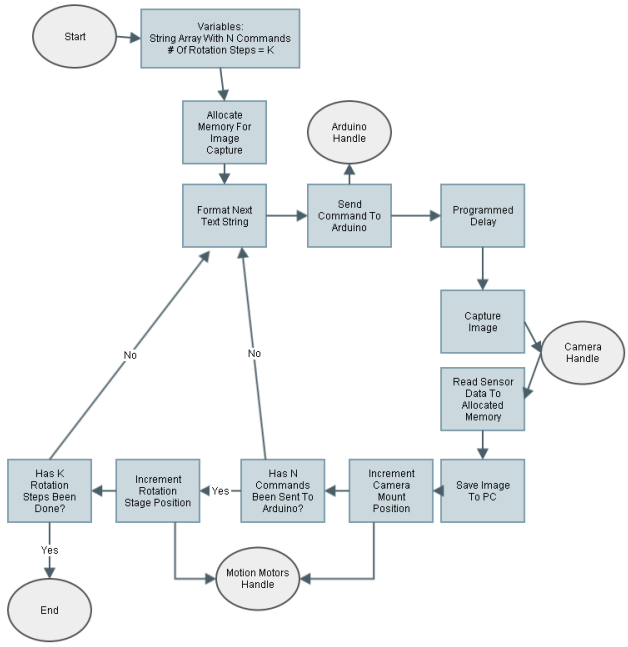

Figure 10.4: Flow chart of the Labview program when the camera is capturing images. The handles are nodes to handle communication with the various hardware. Since motion steps are built in several datasets with various camera positions and rotation stage positions can be done consecutively with the same illumination scheme.

With an exposure time of 500 ms and a pixel rate of 10 megapixels per second, the program uses $\sim$1.6 s from the command is sent to the Arduino until the image is saved on the computer.

Appendix B
Poster Prestented at SYNKNØYT

Results achieved through the work in this thesis was presented on a poster at the Synchrotron and Neutron User Meeting (SYNKNØYT) on Sola in January 2015. The poster presents SAXS tomography, and the major results achieved prior to the conference. It is included in this thesis as an appendix to intrigue potential readers to discover more about SAXS tomography.

Retrieving 3D Orientation Distribution from SAXS Tomorgraphy using Simulated Annealing

Torbjørn Kringeland, Eirik T. B. Skjønsfjell, Håvard Granlund, Kristin Høydalsvik, Dag W. Breiby*

Department of Physics, Norwegian University of Science and Technology, Norway

NTNU – Trondheim
Norwegian University of Science and Technology

We have recently demonstrated mapping experiments using X-ray raster-scanning applied to flake-shaped talc particles embedded in injection-molded isotactic polypropylene(iPP) [1,2]. That mapping approach requires the specimen to be physically cut, which potentially alters the structure and certainly precludes e.g. time-dependent mechanical stress experiments.

Here we present our on-going efforts towards obtaining the full spatially resolved 3D orientation distribution through SAXS tomography. Simulated annealing with constraints of slowly varying structural gradients and approximate sample symmetries, give results agreeing well with results obtained by traditional methods.

RASTER-SCANNING SAXS

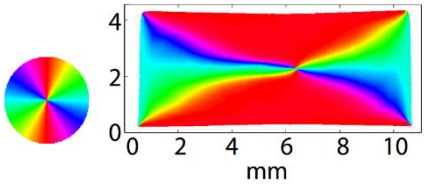

Orientation distribution of the flake talc particles obtained through raster scanning SAXS measurements of a cross section physically cut from the sample. The direction of the surface normal of the talc particles is indicated by the color wheel. These results were later used to compare with orientation distributions retrieved through 3D SAXS tomography experiements.

SAXS TOMOGRAPHY

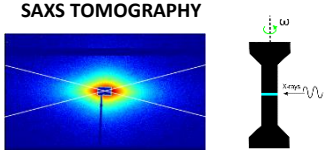

The iPP sample studied was in the shape of a dog bone. For each projection angle ω (green arrow) a line scan was performed across on the dog bone neck, capturing one full SAXS pattern at each position

For each measurement of the SAXS Tomography procedure the horizontal scattering patterns were extracted and used as input for retrieving the structure model.

RETRIEVING ORIENTATION DISTRIBUTION

The best fit to experimental scattering measurements were obtained with the talc particles modeled as oblate ellipsoids, with their surface normal orthogonal to the long axis of the dog bone neck as shown with WAXS and SEM[3]. Then the theoretical scattering intensities were fitted to experimental data.

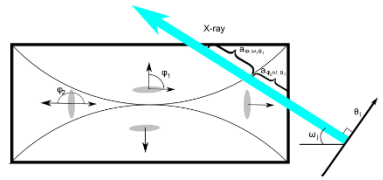

Cross section of the dog bone iPP sample. For each projection angle ω_j the X-ray at position θ_l of the linescan travel a distance $a_{\phi_i\omega_j\theta_l}$ through the regions of the sample containing talc particles (grey ellipses) of different orientations ϕ_i.

A set of *n* possible particle orientations φ_i was chosen with corresponding spatial regions. The scattering intensity at each measurement point (θ_l,ω_j) was taken to be the absolute square of the oriented scattering form factor $I_{\varphi_i\omega_j} = |F_{\varphi_i\omega_j}|^2$ weighted by the distance $a_{\varphi_i\omega_j\theta_l}$ the beam travels through each region of the sample.

$$I_{\theta_l,\omega_j}(Q) = a_{\varphi_1,\theta_l\omega_j} I_{\varphi_1,\omega_j}(Q) + \ldots + a_{\varphi_n,\theta_l\omega_j} I_{\varphi_n,\omega_j}(Q)$$

The orientation distribution was then retrieved through the method of simulated annealing by minimizing the cost function:

$$E = \sum_{\theta,\omega,Q} (I_{Experiment,\theta_l,\omega_j}(Q) - I_{Theoretical,\theta_l,\omega_j}(Q))^2 Q^6$$

While slowly reducing the annealing temperature *T*, favourable orientations of the talc particles at each node of the theoretical sample were chosen subject to the Boltzman probability density function:

$$p_i = e^{-\frac{E}{k_B T}}$$

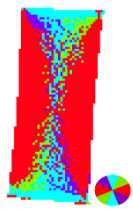

Orientation distribution retrieved through simulated annealing with 4 possible orientations of the talc particles. The direction of the talc surface normals are indicated by the color wheel. Due to less measurement points this reconstruction has lower resolution then the orientation distribution obtained through raster-scanning SAXS. The lack of fine details, and the heavy numerical computations required for the algorithm causes difficulty in increasing the number of possible orientations of the talc particles.

Conclusion

The retrieved orientation distribution shows good resemblance to the results from the raster scan, with all the main overall features present. This method of SAXS tomography however requires no physical cutting of the sample.

[1] H. Granlund *et al.,* Polymer 64(2013) 1877
[2] H. Granlund *et al.,* Journal of Polymer Science B: Polymer Physics 52(2014) 1157-1167
[3] E. T. B. Skjønsfjell, Master Thesis(2013), Norwegian University of Science and Technology

*dag.breiby@ntnu.no